

# Active current sheets and hot flow anomalies in Mercury's bow shock

V. M. Uritsky<sup>1, 2</sup>, J. A. Slavin<sup>3</sup>, S. A. Boardsen<sup>1, 4</sup>, T. Sundberg<sup>1, 5</sup>, J. M. Raines<sup>3</sup>, D. J. Gershman<sup>3</sup>, G. Collinson<sup>1</sup>, D. Sibeck<sup>1</sup>, G. V. Khazanov<sup>1</sup>, B. J. Anderson<sup>6</sup>, and H. Korth<sup>6</sup>

## Abstract.

Hot flow anomalies (HFAs) represent a subset of solar wind discontinuities interacting with collisionless bow shocks. They are typically formed when the normal component of motional (convective) electric field points toward the embedded current sheet on at least one of its sides. The core region of an HFA contains hot and highly deflected ion flows and rather low and turbulent magnetic field. In this paper, we report first observations of HFA-like events at Mercury identified over a course of two planetary years. Using data from the orbital phase of the MErcury Surface, Space ENvironment, GEochemistry, and Ranging (MESSENGER) mission, we identify a representative ensemble of active current sheets magnetically connected to Mercury's bow shock. We show that some of these events exhibit unambiguous magnetic and particle signatures of HFAs similar to those observed earlier at other planets, and present their key physical characteristics. Our analysis suggests that Mercury's bow shock does not only mediate the flow of supersonic solar wind plasma but also provides conditions for local particle acceleration and heating as predicted by previous numerical simulations. Together with earlier observations of HFA activity at Earth, Venus and Saturn, our results confirm that hot flow anomalies are a common property of planetary bow shocks, and show that the characteristic size of these events is of the order of one planetary radius.

## 1. Introduction

The MErcury Surface, Space ENvironment, GEochemistry, and Ranging (MESSENGER) mission [Solomon *et al.*, 2001] provides a deep insight into the structure and dynamics of various plasma regions surrounding the planet. The data reveal a rather active plasma environment which is in many respects unique within our solar system. The magnetosphere of Mercury has been intensively studied in the context of tail and magnetopause reconnection, magnetic flux transport, ULF waves and oscillations, propagating dipolarization fronts, and other phenomena (see e.g. Anderson *et al.* [2008]; Slavin *et al.* [2008, 2009a, c]; Boardsen *et al.* [2009]; Slavin *et al.* [2010]; Sundberg *et al.* [2010, 2012]). It has been shown that the local interplanetary medium surrounding the planet exhibits turbulent variability over both magneto-hydrodynamic and kinetic plasma scales [Korth *et al.*, 2010; Uritsky *et al.*, 2011]. This broadband variability should have a significant impact on the Hermean magne-

<sup>1</sup>NASA Goddard Space Flight Center, Greenbelt, MD, USA

<sup>2</sup>Catholic University of America, Washington, DC, USA

<sup>3</sup>University of Michigan, Ann Arbor, MI, USA

<sup>4</sup>University of Maryland, Baltimore County, Baltimore, MD, USA

<sup>5</sup>Center for Space Physics, Boston University, Boston, MA, USA

<sup>6</sup>John Hopkins University Applied Physics Laboratory, Laurel, MD, USA

39 tosphere and its response to the solar wind driver.

40 The present paper focuses on dynamic discontinuities  
 41 in the Hermean foreshock associated with kinetically active  
 42 current sheets, focusing on the phenomenon of the  
 43 hot flow anomaly (HFA) [Schwartz *et al.*, 1985; Thom-  
 44 sen *et al.*, 1986]. Using the first 180 days of MESSEN-  
 45 GER operation after its orbital insertion, we identify a set  
 46 of interplanetary current sheets magnetically connected  
 47 to the bow shock. We show that some of these current  
 48 sheets exhibit well-defined HFA signatures. We also in-  
 49 vestigate the influence of HFAs on magnetic field vari-  
 50 ability in the adjacent plasma regions and find evidence  
 51 for HFA-triggered ultra low frequency (ULF) waves in  
 52 quasi-parallel shock configurations.

53 The paper is organized as follows. In Section 2, we  
 54 present a concise review of HFA observations in planetary  
 55 bow shocks and summarize magnetic and kinetic signa-  
 56 tures of HFA events. Section 3 describes the methodology  
 57 of our study. Section 4 reports case studies of ten HFA  
 58 events and several examples of active helio current sheets  
 59 not interacting with Mercury’s bow shock. Section 5 re-  
 60 ports statistical properties of the observed events includ-  
 61 ing their location, geometry, duration, relative occurrence  
 62 rates, and other characteristics. Section 6 summarizes  
 63 the obtained results.

## 2. Hot flow anomalies in planetary foreshocks

64 Collisionless planetary bow shocks do not only mediate  
 65 the flow of supersonic plasma but also provide conditions  
 66 for particle acceleration and heating. They can energize,  
 67 decelerate, and deflect solar wind plasma allowing it to  
 68 flow through the magnetosheath and around the mag-  
 69 netosphere [Omididi and Sibeck, 2007]. For certain shock  
 70 geometries, the inflowing solar wind plasma can partly  
 71 return to the upstream region. The interaction between  
 72 this counterstreaming particle population and the inflow-  
 73 ing plasma naturally leads to various plasma instabilities  
 74 and waves which may effectively energize ions and elec-  
 75 trons [Eastwood *et al.*, 2005].

76 For steady solar wind conditions, the large-scale phe-  
 77 nomenology of the foreshock can be organized by the  
 78 angle  $\theta_{B:BS}$  between the upstream magnetic field and  
 79 the bow shock normal, with the quasi-parallel geome-  
 80 try ( $\theta_{B:BS} < 40^\circ$ ) producing the most extended and  
 81 dynamic foreshock system populated by backstreaming  
 82 ions. Changes in the interplanetary magnetic field (IMF)  
 83 direction give rise to a variety of small-scale and/or tran-  
 84 sient foreshock phenomena.

85 HFAs represent a subset of solar wind discontinuities  
 86 (rotational or tangential) interacting with the bow shock  
 87 [Schwartz *et al.*, 1985; Thomsen *et al.*, 1986; Schwartz  
 88 *et al.*, 2000; Billingham *et al.*, 2011]. They are formed  
 89 when the normal component of motional electric field  
 90 points toward the embedded current sheet on at least  
 91 one of its sides [Schwartz *et al.*, 2000]. The core regions of  
 92 HFAs typically contain hot and highly deflected ion flows  
 93 often described by nearly Maxwellian and isotropic parti-  
 94 cle distributions, and rather low and turbulent magnetic  
 95 fields. The direction of bulk plasma flows in HFAs can  
 96 differ significantly from that of the ambient solar wind  
 97 plasma.

98 The first observations of HFAs near Earth were re-  
 99 ported by Schwartz *et al.* [1985] and Thomsen *et al.* [1986]  
 100 based on the data from AMPTE and ISEE and missions.  
 101 Subsequent studies have shown that HFA events appear  
 102 systematically in the terrestrial foreshock, with the aver-  
 103 age occurrence rate of about 3 events per day [Schwartz

104 *et al.*, 2000]. They typically last for a few minutes and  
 105 have spatial scales of the order of one Earth’s radius.  
 106 HFAs can generate considerable perturbations of the dy-  
 107 namic pressure in the upstream solar wind [*Sibeck et al.*,  
 108 1999; *Eastwood et al.*, 2008] and induce significant mag-  
 109 netospheric response, including displacement the nominal  
 110 magnetopause position accompanied by auroral brighten-  
 111 ing [*Sibeck et al.*, 1999], riddling of peripheral boundary  
 112 layers [*Savin et al.*, 2012], transient ULF geomagnetic  
 113 pulsations [*Eastwood et al.*, 2011], and other effects.

114 HFA activity has also been detected at several other  
 115 planets. Mars Global Surveyor observed a HFA-like hot  
 116 diamagnetic cavity upstream of the Martian foreshock  
 117 [*Oieroset et al.*, 2001]. More recently, HFAs were found  
 118 at Saturn’s bow shock based on Cassini data [*Masters*  
 119 *et al.*, 2008, 2009]. Magnetic signatures of HFA events  
 120 at Venus were first reported by *Slavin et al.* [2009b] us-  
 121 ing MESSENGER magnetometer data. The presence of  
 122 HFAs at Venus was later confirmed by magnetic, elec-  
 123 tron and ion observations from Venus Express [*Collinson*  
 124 *et al.*, 2012]. Whilst HFAs have been found throughout  
 125 the solar system, none have been observed at Mercury  
 126 until now.

### 3. Data and methods

#### 3.1. MESSENGER’s orbit and data

127 We investigated the first 180 days of the MESSENGER  
 128 orbital operations (24 March - 19 Sep, 2011) correspond-  
 129 ing to two Mercury years. During this time, MESSEN-  
 130 GER followed a highly elliptical orbit (periapsis  $\sim 200$   
 131 km, apoapsis  $\sim 15,193$  km) enabling observations of a  
 132 significant part of the Mercury’s foreshock both in the  
 133 dawn and dusk sectors. The orbit was inclined  $82.5^\circ$  to  
 134 the equator.

135 The magnetic field data were obtained from the MAG  
 136 magnetometer [*Anderson et al.*, 2007]. The three mag-  
 137 netic field components were measured with a three-axis,  
 138 ring-core fluxgate detector at a typical sampling period  
 139  $\Delta t = 50$  ms. MAG data were used to locate interplane-  
 140 tary active current sheets connected with the Hermean  
 141 bow shock, characterize their dynamics and geometry in  
 142 terms of previous HFA studies, and identify likely in-  
 143 stances of hot flow anomaly events.

144 For some of the events, we also used the data from  
 145 the Fast Imaging Plasma Spectrometer (FIPS, *Andrews*  
 146 *et al.* [2007]). The ion plasma instrument FIPS onboard  
 147 MESSENGER measures ions in the energy per charge  
 148 range of 50 eV/q to 20 keV/q and in the mass per charge  
 149 range of 1 amu/q to 40 amu/q. The FIPS spectral data  
 150 used in this study were averaged over the angular field  
 151 of view of  $1.4 \Omega$ , of which  $0.4 \Omega$  is obscured by the so-  
 152 lar array panels, spacecraft body, and heat shield [*Raines*  
 153 *et al.*, 2011] so angular distribution information is not yet  
 154 available for this data type. The sunshade mounted on  
 155 MESSENGER’s spacecraft body nominally blocks obser-  
 156 vation of the centroid of the solar wind ion velocity space  
 157 distributions by FIPS. The most limiting factor in iden-  
 158 tifying HFA signatures in FIPS observations, however,  
 159 is the time resolution. The time required for FIPS to  
 160 complete an energy-scan is 64 s or 8 s, depending on the  
 161 instrument operational mode.

162 Since the FIPS count rates are a function of plasma  
 163 drift velocity, temperature, and orientation, this data  
 164 should be interpreted with caution. We used FIPS ob-  
 165 servations to look for the presence of ions with energies  
 166 atypical of the expected solar wind, leaving a more de-  
 167 tailed analysis for future studies.

168 The Mercury Solar Orbital (MSO) coordinate system

169 is used for all vector quantities, with  $X_{MSO}$  directed from  
 170 the center of the planet toward the Sun,  $Z_{MSO}$  being  
 171 perpendicular to Mercury’s orbital plane and pointing  
 172 toward the north celestial pole, and  $Y_{MSO}$  completing  
 173 the right-handed system.

### 3.2. Initial event detection

174 Since MESSENGER FIPS is not a reliable source of  
 175 information on transient localized plasma processes at  
 176 Mercury, our event detection was based on MAG data.  
 177 The core regions of HFAs usually contain intervals of con-  
 178 siderable magnetic depression due to the high particle  
 179 pressure exerted by the hot ions. We used this signature  
 180 as the starting point of our search for Mercury’s HFAs,  
 181 followed by the analysis of more subtle features including  
 182 current sheet geometry and detailed B-field variation, re-  
 183 inforced by the analysis of particle data whenever these  
 184 data were available.

185 Fig. 1 illustrates our event detection criteria and the  
 186 associated time intervals. The hot core region of the event  
 187 shown with a yellow rectangle is embedded in a cooler  
 188 plasma medium which is encountered before and after  
 189 the event. These encounters are labeled as the pre-sector  
 190 (blue rectangle) and the post-sector (green rectangle),  
 191 correspondingly. The red magnetic shoulders surround-  
 192 ing the core region are indicative of terrestrial HFA events  
 193 and are a signature of plasma compression caused to an  
 194 expansion of the core HFA region. Such magnetic should-  
 195 ers can be seen in a proto-form in some of the Mercury  
 196 events reported here, although we were unable to find any  
 197 Mercury events with fully developed compression edges.

The intervals of the depressed magnetic field were iden-  
 tified using the smoothed magnetic field  $\hat{B}$

$$\hat{B}(t_i) = \frac{1}{w} \sum_{k=i-w/2}^{i+w/2-1} B(t_k) \quad (1)$$

subjected to the threshold condition

$$\hat{B}(t) < B_{th}, \quad (2)$$

198 where  $w$  is the size of the moving window in time step  
 199 units. In the presence of fast fluctuations (time scale  
 200  $\tau \ll w\Delta t$ ), the smoothed signal  $\hat{B}(t)$  enables more re-  
 201 liable detection of threshold crossings compared to the  
 202 raw magnetic signal. Low-frequency fluctuations with  
 203  $\tau \geq w\Delta t$  require additional attention since they can cause  
 204  $\hat{B}$  to cross the threshold more than once during the same  
 205 event. Such fluctuations are commonly observed in the  
 206 core HFA region where their amplitude can reach the field  
 207 strength in the surrounding plasma (see e.g. *Paschmann*  
 208 *et al.* [1988]). To properly attribute multiple  $B_{th}$  cross-  
 209 ings due to such fluctuations to a single magnetic de-  
 210 pression event, we merged together transient magnetic  
 211 decreases separated by a time gap  $\delta t_g$  of less than 30  
 212 seconds, with the initial smoothing interval of 1 second  
 213 ( $w = 20$ ).

214 After a depressed B-field event is detected, we identi-  
 215 fied three main time intervals corresponding to the ob-  
 216 servations in the core region of the event ( $t \in [t'_0, t''_0]$ ) as  
 217 well as in its pre-sector ( $t \in [t'_1, t''_1]$ ) and the post-sector  
 218 ( $t \in [t'_2, t''_2]$ ). The boundaries of the three intervals were  
 219 calculated as follows (see also Fig. 1):

$$t'_0 = \min\{t | \hat{B}(t) < B_{th}\} \quad (3)$$

$$t''_0 = \max\{t | \hat{B}(t) < B_{th}\} \quad (4)$$

$$t'_1 = t'_0 - \delta t_{e1} - \delta t_{pre} \quad (5)$$

$$t_1'' = t_0' - \delta t_{e1} \quad (6)$$

$$t_2' = t_0'' + \delta t_{e2} \quad (7)$$

$$t_2'' = t_0'' + \delta t_{e2} + \delta t_{post}. \quad (8)$$

220 Here,  $B_{th}$  is the detection threshold,  $\delta t_{pre}$  ( $\delta t_{post}$ ) is  
 221 the duration of the pre (post) sector,  $\delta t_{e1}$  and  $\delta t_{e2}$  are  
 222 the sizes of the edge regions flanking the core region  
 223 from either side [Schwartz, 1995]. The default values  
 224  $\delta t_{pre} = \delta t_{post} = 30$  s and  $\delta t_{e1} = \delta t_{e2} = 10$  s were used for  
 225 the automatic identification of the three regions in the en-  
 226 tire set of the detected events. The region boundaries of  
 227 the events showing clear HFA signatures were then read-  
 228 justed manually taking into account a particular shape  
 229 of the B-field variation. The locations of the events were  
 230 evaluated based on the average MSO position of the core  
 231 region; the event duration  $T$  was calculated from the time  
 232 boundaries of this region:

$$T = t_0'' - t_0' \quad (9)$$

### 3.3. Magnetic geometry

233 For each magnetic field depression event, we computed  
 234 the current sheet normal as the cross product between  
 235 magnetic field before and after the event:

$$\mathbf{n}_{CS} = \pm \mathbf{B}_1 \times \mathbf{B}_2, \quad (10)$$

236 in which  $\mathbf{B}_1$  and  $\mathbf{B}_2$  are the average magnetic field vec-  
 237 tors in the pre- and post- sectors, correspondingly. The  
 238 sign ambiguity was resolved by requiring  $\mathbf{n}_{CS} \cdot \mathbf{V}_{SW} < 0$ ,  
 239 as appropriate for HFA studies [Schwartz *et al.*, 2000].  
 240 The solar wind velocity  $\mathbf{V}_{SW}$  was assumed to be strictly  
 241 anti-sunward and hence parallel to the  $X_{MSO}$  axis. We  
 242 also determined the shortest (projection) distance  $d_{BS}$   
 243 from the core region of the event to the model bow shock  
 244 surface describing the average position of Mercury's bow  
 245 shock for a solar wind fast mode Mach number  $\sim 3$   
 246 [Slavin *et al.*, 2009a]. The same model was used to cal-  
 247 culate the local bow shock normal  $\mathbf{n}_{BS}$  attached to the  
 248 projection point.

249 As stated above, a key HFA formation condition is  
 250 that the solar wind convection (motional) electric field  
 251  $\mathbf{E} = -\mathbf{V}_{SW} \times \mathbf{B}$  points into the underlying discontinuity  
 252 on at least one side (see Fig. 1, right panel). This con-  
 253 dition was verified by computing the angles  $\theta_{E1:CS}$  and  
 254  $\theta_{E2:CS}$  between the current sheet normal and the aver-  
 255 age electric field in respectively pre- and post- sectors.  
 256 We also computed the angle  $\theta_{B1:B2}$  between the mag-  
 257 netic vectors  $\mathbf{B}_1$  and  $\mathbf{B}_2$ , the angles  $\theta_{B1:BS}$  and  $\theta_{B2:BS}$   
 258 created by these vectors with the local bow shock normal  
 259  $\mathbf{n}_{BS}$ , the angle  $\theta_{CS:BS}$  between  $\mathbf{n}_{CS}$  and  $\mathbf{n}_{BS}$ , and the  
 260 angles  $\theta_{SW:CS}$  and  $\theta_{SW:BS}$  between the solar wind flow  
 261 direction and each of the two normals.

The magnitude of the events was measured by two  
 parameters – the normalized field jump across the current  
 sheet [Schwartz *et al.*, 2000],

$$\Delta B_{12} = \frac{|B_1 - B_2|}{\max(B_1, B_2)}, \quad (11)$$

and the maximum normalized amplitude of the field de-  
 crease in the core region,

$$\Delta B_0 = \frac{B_{12max} - B_{0min}}{\max(B_1, B_2)}, \quad (12)$$

262 in which  $B_{12max}$  is the largest B-field magnitude observed  
 263 in both pre- and post- sectors and  $B_{0min}$  is the smallest  
 264 field inside the core region.

265 To quantify the efficiency of the current sheet - bow  
 266 shock interaction, we estimated the ratio between the  
 267 transit velocity of the event,  $V_{tr}$ , and the local gyroveloc-  
 268 ity of solar wind protons,  $V_g$  [Schwartz *et al.*, 1983, 2000]:

$$\left| \frac{V_{tr}}{V_g} \right|_{1,2} = \frac{\cos(\theta_{SW:CS})}{2 \cos(\theta_{SW:CS}) \sin(\theta_{B1,2:CS}) \sin(\theta_{CS:BS})} \quad (13)$$

269 where indexes 1 and 2 apply to pre- and post sectors as  
 270 usual.

271 The parameters listed above were used to select candi-  
 272 date HFA events from the automatically detected set of  
 273 magnetic field depression events satisfying the threshold  
 274 condition (2). Final classification of events involved man-  
 275 ual validation focused on the detailed shape of the mag-  
 276 netic field variation before, during and after the event,  
 277 statistical properties of kinetic-scale magnetic field fluc-  
 278 tuations indicative of an ion heating, and ion energy spec-  
 279 tra.

### 3.4. Fluctuation analysis

280 Our analysis of MESSENGER's first flyby of Mercury  
 281 has shown that the Hermean magnetosphere, as well as  
 282 the surrounding region, are affected by non-MHD effects  
 283 introduced by finite sizes of cyclotron orbits of the con-  
 284 stituting ion species [Uritsky *et al.*, 2011]. Kinetic-scale  
 285 magnetic fluctuations seems to play a significant role in  
 286 Mercury's magnetosphere up to the largest resolvable  
 287 timescale dictated by the signal nonstationarity.

288 To investigate statistical properties of magnetic field  
 289 fluctuations associated with the magnetic depression  
 290 events, we used the method of higher order structure  
 291 function (SF) generalized by Uritsky *et al.* [2011] for the  
 292 case of strongly nonstationary signals. Using this tool,  
 293 we compared magnetic turbulence inside and outside the  
 294 detected events, and evaluated the ion crossover scale  
 295 separating fluid-like and kinetic-like modes of behavior  
 296 of solar wind plasma.

The time-domain higher-order SF is defined as

$$S_q(\tau) = \langle |\delta B_\tau|^q \rangle, \quad (14)$$

297 in which  $\delta B_\tau$  are the differences of the studied turbu-  
 298 lent field  $B$  measured at time lag  $\tau$ ,  $\langle \cdot \rangle$  denotes averaging  
 299 over all pairs of points separated by this lag, and  $q$  is  
 300 the order. The SF exponents  $\zeta_q$  estimated from the scal-  
 301 ing ansatz  $S_q(\tau) \propto \tau^{\zeta_q}$  provide a detailed description of  
 302 the turbulent regime under study. The second-order SF  
 303  $S_2(\tau)$  plays a special role in statistical mechanics of tur-  
 304 bulent media as a proxy to the band-integrated wavenum-  
 305 ber Fourier spectrum [Biskamp, 2003]. The power-law  
 306 exponent  $\beta$  of the spectrum is related to the SF expo-  
 307 nent through  $\zeta_2 = \beta - 1$  under the assumption of linear  
 308 space-time coupling.

309 In order to study transient and/or spatially inhomoge-  
 310 neous solar wind fluctuations, we used local SF estimates  
 311 made within a sliding window of width  $W$ . For each slid-  
 312 ing window position, we computed a set of temporal SFs  
 313 according to eq. 14, with  $q = 2$  and  $\tau < W/2$ . The  
 314 time-dependent shape of the resulting two-dimensional  
 315 windowed structure function  $S_2(\tau, t)$  was represented as  
 316 a continuous second-order time-period scalogram  $\zeta_2(\tau, t)$ :

$$\zeta_2(\tau, t) = \frac{\partial \log \left[ \frac{1}{W-\tau+1} \sum_{t'=t-W/2}^{t+W/2-\tau} \left| \tilde{B}(t') - \tilde{B}(t'+\tau) \right|^2 \right]}{\partial \log \tau}. \quad (15)$$

317 Here,  $\tilde{B}(t') = B(t') - \phi(t, t', \Delta)$  is the locally de-  
 318 trended magnetic signal, with  $\phi$  being the quadratic  
 319 polynomial fit to  $B$  over the windowed time interval  
 320  $t' \in [t - W/2, t + W/2]$ ,  $\tau$  is the time scale, and  $t$  is  
 321 the running time variable reflecting the central position  
 322 of the sliding window. We used quadratic detrending  
 323 as the simplest way to compensate for the nonstationary  
 324 trends reflecting spatial inhomogeneity of the tra-  
 325 versed plasma structures. Following the approach pro-  
 326 posed by *Matthaeus and Goldstein* [1982], the stationarity  
 327 of the signal was verified based on the ergodic theorem  
 328 for weakly stationary random processes [*Monin and Ya-*  
 329 *glom*, 1975]. The partial derivative in the above equation  
 330 is evaluated from the local least-square linear regression  
 331 slope of the  $S_2(\tau)$  dependence in the log - log coordinates  
 332 for each sliding window.

333 The continuous SF scalogram technique defined by eq.  
 334 (15) is essentially different from the widely used wavelet-  
 335 based of Fourier transform-based dynamic spectrogram  
 336 techniques (see e.g. *Alexandrova et al.* [2006]; *Boardsen*  
 337 *et al.* [2009]) as it allows analysis of temporal variations of  
 338 the scaling structure of magnetic fluctuations rather than  
 339 their spectral amplitudes. As shown in the next section,  
 340 the SF scalogram provides evidence for drastically differ-  
 341 ent turbulent plasma environments inside and outside the  
 342 HFA events. In the absence of relevant particle data, this  
 343 piece of information turns out to be particularly useful.

344 Using the Taylor frozen-in flow condition which is usu-  
 345 ally fulfilled in the solar wind (see e.g. *Matthaeus et al.*  
 346 [2005] and references therein) and assuming that the up-  
 347 per spatial scale of ion-kinetic turbulent regime is con-  
 348 trolled by finite Larmor radius effects [*Schekochihin et al.*,  
 349 2007], the ion gyro radius  $\rho_i$  and the ion temperature  $T_i$   
 350 can be evaluated through [*Uritsky et al.*, 2011]

$$\rho_i \approx V_{SW} \tau_i / 2\pi, \quad (16)$$

$$T_i \approx m_i (V_{SW} \tau_i / \tau_{ci})^2, \quad (17)$$

351 in which  $\tau_i$  is the largest temporal scale at which the  
 352 power-law slope of locally estimated SF is consistent with  
 353 ion-kinetic  $\zeta_2$  values, typically in the range 1.3 - 1.5 de-  
 354 pending on the underlying dispersive wave mode (usually  
 355 kinetic Alfvén waves or whistler branches with secondary  
 356 lower hybrid activity), and the turbulence type (i.e., a  
 357 weak or strong) – see, e.g., *Yordanova et al.* [2008]; *East-*  
 358 *wood et al.* [2009]; *Sahraoui et al.* [2009]. Compressional  
 359 corrections further increase the kinetic-scale exponents  
 360 [*Alexandrova et al.*, 2008]. For practical purposes, it is  
 361 sufficient to use a simplified condition  $\zeta_2 \approx 1$  to identify  
 362  $\tau_i$  [*Uritsky et al.*, 2011].

#### 4. Case studies

363 In this section, we present a subset of magnetic field  
 364 depression events exhibiting magnetic and kinetic HFAs  
 365 signatures, as compared to several non-HFA events as-  
 366 sociated with passages of helio current sheets (HCSs).  
 367 All the events were initially detected automatically, after  
 368 which the boundaries of their pre-, post- and core sectors  
 369 were adjusted manually to better match their magnetic

370 field profiles not captured by the default definitions. The  
 371 parameters of the HFA and HCS events are summarized  
 372 in Tables 1 and 2, correspondingly.

#### 4.1. HFA-like events

373 Ten HFA-like events were identified during the studied  
 374 180 day period. Below we provide detailed portraits of  
 375 each of these events.

376 **Event 1** (Fig. 2, left) occurred on April 16, 2011 just  
 377 outside of the bow shock boundary, close to the noon-  
 378 midnight meridian plane. The event was centered at  
 379 about 19:00:22 UT and characterized by a normal moti-  
 380 onal electric field component pointed toward the cur-  
 381 rent sheet in the post sector only ( $\theta_{E2:CS} = 151^\circ$ ). Both  
 382 leading and trailing edges of the event showed mild mag-  
 383 netic field enhancements, with the trailing edge lasting  
 384 twice as long compared to the leading edge (respectively  
 385  $\sim 3$  and  $\sim 7$  s, or  $\sim 1400$  and  $3200$  km at a nominal  
 386 solar wind speed of  $450$  km/s). The more pronounced  
 387 trailing edge may reflect a more the favorable E-field ori-  
 388 entation on that side [Thomsen *et al.*, 1993]. The de-  
 389 scribed features coexist with an irregular ULF oscillation  
 390 which precludes their more accurate analysis. The event  
 391 shows a small B-field rotation angle  $\theta_{B1:B2}$  of  $\sim 20^\circ$  and a  
 392 quasi-parallel magnetic field alignment relative to the lo-  
 393 cal bow shock normal. The core region of the event shows  
 394 significantly reduced B-field magnitude ( $\Delta B_0 \sim 1.1$ ) last-  
 395 ing for about 20 s, and a noticeably sharper trailing wall  
 396 consistent with stronger plasma compression expected on  
 397 the side exposed to the inwardly directed motional elec-  
 398 tric field. The normal magnetic field is close to zero and  
 399 stays fairly constant inside the core region, and is 3-5  
 400 times lower than the tangential B-field both in the core  
 401 and in the surrounding plasma environment, an indica-  
 402 tion of a nearly perpendicular shock [Paschmann *et al.*,  
 403 1988]. The jump in the tangential field  $B_T$  by a factor  
 404 of  $\sim 2.5$  at the inner wall of the trailing edge implies a  
 405 jump in the plasma density as required for such shocks.

406 The core of event 1 shows a very clear and well-  
 407 localized enhancement of kinetic-scale magnetic turbu-  
 408 lence (bottom panel), with the ion kinetic crossover  
 409 marked by the yellow color in the chosen color coding ris-  
 410 ing up to  $\tau_i \sim 2$  s during the event. The kinetic crossover  
 411 is not resolved by the MAG instrument in the ambient  
 412 plasma region, suggesting that  $\tau_i$  was increased by at  
 413 least a factor of 10 in the core of this HFA. The observed  
 414 change implies a proportional increase of the proton gyro  
 415 radius which can not be explained by the much more  
 416 modest drop of the average field magnitude during the  
 417 event, unless it was accompanied by a plasma heating.  
 418 By using eq. (17) with  $V_{SW} = 450$  km/s, we estimate  
 419 the proton temperature in the core region to be  $\sim 95$   
 420 eV, or about  $1.1 \times 10^6$  K, which is a factor of 5 greater  
 421 than typical solar wind temperature. The obtained value  
 422 is in agreement with the temperatures observed in the  
 423 central region of terrestrial HFAs ( $\sim 10^6 - 10^7$  K [Thom-  
 424 sen *et al.*, 1988; Paschmann *et al.*, 1988; Schwartz *et al.*,  
 425 2000]), and is three times higher than the typical proton  
 426 temperature in the ambient solar wind plasma at Mer-  
 427 cury's orbit [Baker *et al.*, 2009; Uritsky *et al.*, 2011].

428 Event 1 is supported by relevant particle observations.  
 429 FIPS spectra show clear particle energization associated  
 430 with this HFA. The FIPS spectra were averaged over the  
 431 instruments angular field of view,  $1.4 \Omega$ , of which  $0.4$  was  
 432 obscured. During the presented observation interval, the  
 433 FIPS  $E/q$  range was set to  $0.046 - 13.60$  keV/q, and the  
 434 scan time was 64 s. The color-coded plot in Fig. 3 (top  
 435 panel) shows the energy versus time spectrogram of the  
 436 averaged differential proton flux during event 1. There

437 is a noticeable increase in the ion energy both preceding  
 438 and following the HFA, with the strongest energization  
 439 roughly consistent with the position of the core region  
 440 of the event. Although the low time resolution of FIPS  
 441 data prevents a more detailed analysis of the structure  
 442 of this event, it is sufficient for determining that a hotter  
 443 ion population may be present at the HFA. The arrival  
 444 directions measured by FIPS are consistent with the ap-  
 445 pearance of a beam-like flow, although the statistics are  
 446 too limited to be analyzed quantitatively.

447 The angle between the motional electric field and the  
 448 current sheet stayed almost constant in the pre-sector of  
 449 event 1 (Fig. 2, left). It began to show transient de-  
 450 partures from the original value of  $\sim 150$  degrees in the  
 451 post-sector of the event with the motional field being al-  
 452 most parallel to the current sheet plane on several brief  
 453 occasions. These rotations had an irregular recurrence  
 454 period of  $\sim 7 - 15$ s and could be an indication of un-  
 455 stable plasma conditions which in turn led to the strong  
 456 ULF wave oscillations seen a few seconds after the event.  
 457 These low frequency waves had a period of  $\sim 10$  seconds  
 458 (0.1 Hz), wave amplitude of  $\sim 5-10$  nT, a low level of  
 459 coherence, and a predominant left-hand polarization. A  
 460 comparison of the minimum variance direction and the  
 461 field-aligned direction suggests a wave normal angle of  $\sim$   
 462  $10-15$  deg. A second high frequency pulsation, around  
 463  $3-4$  Hz, was present simultaneously. These waves were  
 464 also left-hand circularly polarized (Fig. 3, bottom group  
 465 of panel) and were observed from the edge of the core  
 466 region until  $\sim 19:07$  UT. The wave intensity was varying  
 467 on short time-scales and had a behavior similar to that  
 468 of the electromagnetic ion-cyclotron waves. As the mag-  
 469 netic field in this region is nearly parallel with the bow  
 470 shock normal, the wave excitation may be driven by back-  
 471 streaming ions from the bow shock, along with escaping  
 472 hot ions from the HFA, which also is consistent with the  
 473 hot ion population observed over the wave interval.

474 **Event 2** (Fig. 2, right) occurred about 9 minutes after  
 475 event 1 and also showed a significant reduction of mag-  
 476 netic field strength in the core region ( $\Delta B_0 \sim 0.8$ ). The  
 477 fairly small normalized change in the B-field across the  
 478 current sheet ( $\Delta_{12} < 0.1$ ) makes it difficult to interpret  
 479 the discontinuity underlying this event as a clean tan-  
 480 gential discontinuity (TD). The current sheet features a  
 481 rather small  $\theta_{CS:BS}$  angle of less than 10 degrees revealing  
 482 its parallel alignment with the bow shock surface. Both  
 483 parameters are the lowest for the presented collection of  
 484 events, and are not typical for terrestrial HFAs. In ad-  
 485 dition, the event features a nearly perpendicular geome-  
 486 try ( $\theta_{B1,2:BS} \approx 90^\circ$ ) with no strong magnetic connection  
 487 with the bow shock. In spite of the unusual orienta-  
 488 tion, event 2 has a consistent “toward” orientation of the  
 489 motional electric field both in the pre- and post-sectors  
 490 resulting in well-defined and almost symmetric trailing  
 491 and leading edges revealing compressed plasma regions  
 492 around the anomaly. On the other hand, the E-field di-  
 493 rection outside of the core region remains effectively un-  
 494 changed. The observed  $\theta_{E:CS}$  dynamics could be consis-  
 495 tent with an interplanetary discontinuity surrounded by  
 496 relatively quiet plasma regions, and is not characteristic  
 497 of strong HFAs which tend to be embedded in a more vi-  
 498 olent foreshock environment. The SF scalogram shows a  
 499 mild increase of the ion-kinetic time scale at the leading  
 500 edge of the event (from 0.3 to  $\sim 2$  s), with the estimated  
 501 core region temperature of about 30 eV suggesting only a  
 502 marginal heating. This is consistent with the rather large  
 503 ratio  $|V_{tr}/V_g| \sim 3$  at both sides of the event. Based on  
 504 this estimate, the event can be classified as a moderately  
 505 active HFA-like current sheet which moved too fast to

506 experience any significant gyrokinetic heating.

507 **Event 3** (Fig. 4, left) was observed at 04:50:30-  
 508 04:51:00 UT on April 20, 2011. It features more pro-  
 509 nounced HFA signatures compared to the previous event.  
 510 Event 3, as well the rest of the events discussed below in  
 511 this subsection, had properly oriented motional electric  
 512 fields pointing toward the current sheet on either sides  
 513 of the event. The event shows a fairly large difference  
 514 in the B-field magnitude in the pre- and post-sectors de-  
 515 scribed by  $\Delta B_{12} \sim 0.4$  making it an almost certain TD  
 516 [Neugebauer *et al.*, 1984]. The magnetic field undergoes  
 517 several rapid directional changes inside the core region re-  
 518 vealing multiple embedded current sheets. A significant  
 519 normal magnetic field component associated with these  
 520 changes signals an arbitrary orientation of the small-scale  
 521 current sheets relative to the main current sheet. The  
 522 finest temporal scale of the embedded discontinuities is  
 523 of the order of a tenth of a second which translates into  
 524 the spatial scale of  $\sim 40$ -50 km for typical solar wind  
 525 conditions. These structures have a kinetic origin and  
 526 could be supported by several distinct ion populations,  
 527 deflected at different angles by the bow shock boundary.  
 528 The intermittent structure of the discussed event resem-  
 529 bles short large-amplitude magnetic structures (SLAMS)  
 530 which are commonly observed at a quasi-parallel terres-  
 531 trial bow shock [Schwartz *et al.*, 1992], and recently in the  
 532 foreshock of Venus [Collinson *et al.*, 2012]. The structure  
 533 of event 3 is similar to SLAMS embedded within a bound-  
 534 ary with regions of considerable heating and deceleration.  
 535 The time scale, polarization parameters, and other char-  
 536 acteristics of SLAMS observed at Earth a suggestive of  
 537 their growth out of ULF wave packets [Schwartz *et al.*,  
 538 1992] which are commonly found in HFA cavities. The  
 539 wave field of less evolved HFAs can be quite complex  
 540 [Tjulin *et al.*, 2008]. Event 3 is likely to belong to this  
 541 category because of its location near the subsolar point  
 542 suggesting a recent initial interaction with Hermean bow  
 543 shock. All other HFA events considered in this section  
 544 were located further downstream and therefore had more  
 545 time to develop, which may explain their less turbulent  
 546 core region environment.

547 The core region of event 3 has well-developed edges  
 548 with sharp field gradients indicative of strong plasma  
 549 compression. In the wake of the event, there is a co-  
 550 herent oscillatory activity with a frequency of about 2  
 551 Hz which is  $\sim 10$  times higher than the local proton gyro  
 552 frequency. The mechanism of this post-sector wave activ-  
 553 ity which we saw in several other Hermean HFAs remains  
 554 to be understood. The SF scalogram shows a dramatic  
 555 increase of the ion crossover scale in the core region of  
 556 the event, up to  $\sim 2$  s near the inner side of the trailing  
 557 edge. When plugged into eq.(17), this fluctuation scale  
 558 predicts a proton temperature of  $\sim 470$  eV, or about  
 559  $5.5 \times 10^6$  K, which is comparable with typical HFAs seen  
 560 at Earth. The scalogram also suggests that the heated,  
 561 and presumably strongly deflected core particle popula-  
 562 tion “leaks” through the trailing edge into the portion  
 563 of the post-sector adjacent to the event. If this leakage  
 564 does take place, it can play an important part in the ex-  
 565 citation of a plasma instability underlying the 2 Hz wave  
 566 oscillation in this sector.

567 During event 3, FIPS operated in its fast scanning  
 568 mode ensuring a 8-second time resolution. At this sam-  
 569 pling time, it is possible to match the heated plasma re-  
 570 gion with the magnetic signature of the HFA (Fig. 5). In  
 571 can be seen that the event is associated with a broadened  
 572 range of energies ( $\sim 100$  eV - 10 keV) taking place in the  
 573 core region and at the trailing current sheet. The pre-  
 574 sented FIPS spectrogram indicates a substantial plasma

575 heating.

576 **Event 4** (Fig. 4, right) occurred at about 03:52:45  
 577 - 03:53:00 UT on April 21, 2011. Despite the symmet-  
 578 ric E-field geometry providing favorable HFA conditions  
 579 on either side of the cavity, only the leading edge of this  
 580 event has a noticeable compression which lasted for  $\sim 3$   
 581 s (or approximately 1350 km in size for  $V_{SW} = 450$   
 582 km/s). The magnetic field depression in the core re-  
 583 gions is characterized by a relatively small normalized  
 584 magnitude  $\Delta B_0 \sim 0.5$ . The event shows a moderate  
 585 enhancement of kinetic-scale turbulence which neverthe-  
 586 less caused a sizable jump in  $\tau_i$  from  $\sim 0.2$  s in the late  
 587 pre-sector to more than 1 s in the core region. The pre-  
 588 dicted pre-sector temperature is an order of magnitude  
 589 lower than expected for an ambient solar wind and may  
 590 indicate a presence of strongly decelerated ions in front  
 591 of the propagating event. The remarkably stable electric  
 592 field angle  $\theta_{E:CS}$  observed prior to the arrival of the event  
 593 agrees with this interpretation pointing at a thermody-  
 594 namically stable and unperturbed plasma medium.

595 In the middle of the core region of event 4, there is  
 596 an isolated pillar of enhanced magnetic field magnitude  
 597 which is considerably larger than the spikes observed in  
 598 the core region of event 3. Singular embedded structures  
 599 such as the one identified inside event 4 are indicative of a  
 600 partial flow recovery and are often observed in terrestrial  
 601 HFAs [Schwartz, 1995]. More recently, they have been  
 602 found at Venus [Slavin *et al.*, 2009a].

603 Events 5 and 6 (Fig. 6) were both observed on May 04  
 604 2012 during two subsequent MESSENGER orbits. The  
 605 events were centered at 06:08:30 UT and 18:26:40 UT,  
 606 correspondingly. In spite of the 12-hour time separation,  
 607 the events have much in common. Their location is quite  
 608 close to the equatorial plane in the dawn foreshock region  
 609 with a quasi-parallel magnetic field geometry ( $\theta_{B:BS} \sim$   
 610  $20 - 50^\circ$ ), and both events show classical compression  
 611 signatures at the leading and trailing edges consistent  
 612 with a convection E-field pointed inward on either side of  
 613 the current sheets. The compressed edges are clearly seen  
 614 in event 5 but are also identifiable in event 6. Both events  
 615 show pronounced transient heating signatures in the SF  
 616 scalogram coinciding with the core regions of the events,  
 617 and a similar magnetic field rotation angle of  $60 - 70$   
 618 degrees.

619 **Event 6** (Fig. 6, right) exhibits a strong transient en-  
 620 hancement of the B-field magnitude in the middle of the  
 621 core region analogous to that of event 4 (Fig. 4, right).  
 622 The peak of this brief enhancement lasts for  $\sim 0.7$  s, sug-  
 623 gesting a spatial scale of a few hundred kilometers. Based  
 624 on the  $\tau_i$  estimate from the SF scalogram, the tempera-  
 625 ture of the plasma environment surrounding this struc-  
 626 ture is of the order of 50 eV, with a proton gyro radius  
 627 of  $\sim 140$  km. The discussed set of properties, especially  
 628 the sharp inner walls of the core region, should be of ki-  
 629 netic origin. Interestingly enough, event 5 (Fig. 6, left)  
 630 shows an even more significant variation of the magnetic  
 631 field magnitude in the core region which, however, has  
 632 a longer temporal scale ( $\sim 2$  s) and a larger estimated  
 633 size ( $\sim 900$  km) compared to event 6. According to the  
 634 SF scalogram, the core region temperature inside event  
 635 5 rises up to 360 eV, but due to the stronger average  
 636 B-field, the predicted proton gyro scale is roughly the  
 637 same as during event 6. Overall, events 5 and 6 are in a  
 638 qualitative agreement with the observations of HFAs at  
 639 Earth's quasi-parallel bow shock.

640 Event 6 has a quite short core region duration ( $T = 6$   
 641 s) although its travel- to gyro velocity ratio is fairly low  
 642 ( $\sim 0.42$  in the pre-sector). The low bow shock sliding ve-  
 643 locity could explain the efficient heating of this compact

644 event.

645 **Event 7** was observed on May 07 2011 between about  
 646 04:43:40 - 04:48:30 (Fig. 7, left). It has the longest dura-  
 647 tion among the detected HFA events, with the core region  
 648 passage lasting for almost 5 min. The “toward” motional  
 649 electric field is observed in the pre-sector which also fea-  
 650 tures a small but distinct compression edge. The plasma  
 651 content of the core region is significantly nonuniform. Ac-  
 652 cording to the fluctuation scalogram, the leading edge is  
 653 rather sharp and is associated with a transition from a  
 654 high-frequency spiky noise (possibly of electrostatic ori-  
 655 gin [*Singh et al.*, 2007]) outside the event to a cross-scale  
 656 turbulent cascade observed inside. At the trailing edge,  
 657 the scaling structure of magnetic fluctuations changes in  
 658 reverse order, but the time of this transition is not well  
 659 defined. Irregular variations of the fluid-kinetic crossover  
 660 seen inside the core region confirm the presence of multi-  
 661 ple hot plasma layers separated by a substantially cooler  
 662 plasma. The hottest ion population is observed near the  
 663 trailing edge where  $\tau_i$  reaches 1.0 - 2.0 s, which using eq.  
 664 17 predicts a temperature range of  $4 - 11 \times 10^5$  K, or 30  
 665 - 95 eV.

666 Some of the magnetic field depressions inside the core  
 667 region of event 7 are associated with considerable changes  
 668 in the magnetic field orientation signaling small-scale cur-  
 669 rent sheets. One of such embedded structures was en-  
 670 countered at 04:46:30. It was accompanied by an abrupt  
 671 50-degree change of the  $\theta_B$  angle. Another rotation for  
 672 an even larger  $\sim 75$  degrees angle was detected at about  
 673 04:47:00. These compact current-carrying structures can  
 674 be sites of separate heating events. Some of the local min-  
 675 ima in the B-field magnitude are matched by substantial  
 676 decreases of the normal component hinting at tangential  
 677 discontinuities. The mutual arrangement of the embed-  
 678 ded current sheets does not show stable periodicity and  
 679 is likely to be shaped by MHD turbulence.

680 Event 7 is characterized by a weak connection to the  
 681 bow shock both before and after the core region, with  
 682  $\theta_{B1:BS} \approx \theta_{B2:BS} \sim 70$  degrees, and is located rela-  
 683 tively far from the nominal bow shock boundary  
 684 ( $d_{BS} \sim 1.6R_M$ ). The magnetic field rotation between  
 685 the pre- and post-sectors is unremarkable. Assuming  
 686 that the hot core region is passively advected with the  
 687 nominal solar wind speed and taking into account the  
 688 angle  $\theta_{SW:CS}$  between the solar wind flow and the cur-  
 689 rent sheet, the thickness of this HFA is about  $7 R_M$ . The  
 690 velocity ratio  $|V_{tr}/V_g|$  is estimated to be  $\sim 0.35$  before  
 691 and after the event, implying that the transit speed was  
 692 sufficiently slow for the ions to be transported along the  
 693 shock. The long interaction time could help the develop-  
 694 ment of this event in the quasi-perpendicular bow shock  
 695 geometry untypical for HFAs.

696 Ion energization during event 7 is confirmed by FIPS  
 697 measurements (Fig. 8). The most energetic ion popula-  
 698 tion was encountered close to the center of the core re-  
 699 gion, between 04:46:10 and 04:47:25. The heated plasma  
 700 extends beyond the trailing event edge into the post-  
 701 sector, in agreement with the washed-out trailing edge  
 702 position on the SF scalogram as discussed above.

703 **Event 8** was observed on August 13, 2011 (Fig. 7,  
 704 right), with the core region center at  $\sim 04:28:00$ . It fea-  
 705 tures favorable orientation of the motional E-field at both  
 706 sides of the current sheet. The post-sector shows a some-  
 707 what better magnetic connection with the bow shock  
 708 compared to the pre-sector. The SF scalogram demon-  
 709 strates a clear-cut fluctuation signature of ion tempera-  
 710 ture enhancement similar to that seen in other Hermean  
 711 HFAs. The core region temperature increase is likely to  
 712 be small, of the order of 20-30 eV, but it is statistically

713 significant compared to the the ambient plasma tempera-  
 714 ture. The compression shoulders are apparently missing.  
 715 Based on these signatures, event 8 could be classified as  
 716 a proto-HFA event rather than a fully developed HFA,  
 717 analogous to event 2 shown in Fig. 2 (right).

718 The FIPS energy spectrogram of event 8 (Fig. 9) is  
 719 much like that of event 3. The spectrogram was obtained  
 720 in the fast scanning mode and demonstrates a wide range  
 721 of ion energies ranging from 100 eV to about 2 keV. This  
 722 behavior is atypical for the solar wind and is consistent  
 723 with the presence of a local plasma heating mechanism.  
 724 The hotter post-sector of event 8 is in an agreement with  
 725 the asymmetric shape of the turbulence scalogram pre-  
 726 dicting a larger ion kinetic scale in that sector compared  
 727 to the pre-sector.

728 **Event 9** (Fig. 10, left) shows a “toward” E-field ori-  
 729 entation on both sides of the core region and has ap-  
 730 proximately that same duration as event 8. Event 9  
 731 has a consistent non-zero  $B_N$  component in the core re-  
 732 gion, comparable with the tangential magnetic field, and  
 733 demonstrates several B-field reductions inside the core  
 734 region reminiscent of the embedded current sheet struc-  
 735 tures in event 7. However, event 9 involves a significant  
 736 net magnetic field rotation of about 50 degrees. It shows  
 737 no identifiable compression regions, although its trail-  
 738 ing edge is rather sharp implying a thin current-carrying  
 739 plasma layer. The post-sector of event 9 has a consid-  
 740 erably weaker magnetic connection with the bow shock  
 741 compared to the pre-sector, which leaves open the ques-  
 742 tion of whether the trailing current sheet is due to an  
 743 HFA-driven plasma expansion or is a pre-existing solar  
 744 wind structure. The event was accompanied by a modest  
 745 B-field depression ( $\Delta B_0 \sim 0.37$ ) but a clearly-manifested  
 746 increase of the ion-kinetic crossover time from  $\tau_i \leq 0.6$  s  
 747 at the inner edge of the core region to about  $\tau_i \sim 1.3$  at  
 748 its center, implying a 10-fold temperature growth.

749 **Event 10** took place at about 02:22:45 of Aug 13, 2011  
 750 (Fig. 10, right). It shows the shortest duration ( $\Delta t \sim 4$   
 751 s) over the entire set of HFA-like current sheets reported  
 752 here, and is also characterized by the smallest relative  
 753 reduction of the B-field magnitude. A clear ion energiza-  
 754 tion footprint can be seen on the scalogram plot, with the  
 755 ion-kinetic scaling extending up to  $\tau_i \sim 2$  s inside the core  
 756 region. The ion temperature predicted for the crossover  
 757 time and the observed field magnitude is  $1.1 \times 10^6$  K,  
 758 or 90-100 eV. A relatively small ( $\sim 32$  degrees) but con-  
 759 sistent magnetic field rotation observed outside the core  
 760 region suggests that event 10 is embedded into a current  
 761 sheet. This current sheet is nearly perpendicular to the  
 762 nominal bow shock surface ( $\theta_{CS:BS} \sim 100$  degrees) and  
 763 has a stable magnetic connection with the bow shock in  
 764 the pre-sector region. A rather low velocity ratio in the  
 765 post-sector is consistent with the asymmetric shape of  
 766 the magnetic signature which shows a more pronounced  
 767 B-field decrease at the inner side of the core / post-sector  
 768 boundary. This sharp decrease suggests a small-scale cur-  
 769 rent layer, possibly formed by hot expanding plasma of  
 770 the core region, incorporated into the main current sheet.  
 771 The embedded current system affects predominantly the  
 772 tangential magnetic field component and leaves  $B_N$  un-  
 773 changed. It is also associated with a jump in the motional  
 774 electric field direction, with a “toward” orientation on  
 775 both sides. Based on these signatures, the trailing edge  
 776 of event 10 should provide a particularly efficient heating  
 777 environment. The remote location of event 10 relative to  
 778 the bow shock ( $d_{BS} \sim 1.9R_M$ ) could explain its intermit-  
 779 tent nature.

#### 4.2. Non-HFA active current sheets

In addition to the HFA-like events described above, our algorithm has detected nine HCS events. Table 2 provides a summary of physical and geometric characteristics of these events. Four of them (Fig. 11-12) are chosen to illustrate the distinction between HCS and HFA observations at Mercury's bow shock. These four non-HFA current sheets failed to develop HFA signatures by the time of their encounter with MESSENGER despite the proper (toward) orientation of the pre- and post-sector convection electric fields and a significant B-field depression in the middle.

The HCS events shown in Fig. 11-12 have no compressed leading or trailing edges characteristic of HFAs. They feature a large-scale reorganization of the field geometry across the current sheet. The directional E-field change across these current sheets is likely to represent a large-scale solar wind structure rather than a local plasma kinetics, and is more indicative of freely propagating helio current sheet than of kinetically active current sheet interacting with the bow shock. All non-HFA helio current sheets were observed at a larger distance from the model bow shock compared to all but one HFAs on our list. The majority of the HCS events featured quasi-perpendicular magnetic field orientation relative to the local bow shock normal. These current sheets were likely to be magnetically disconnected from the bow shock, which prevented their evolution into HFAs.

The fluctuation signatures of HCS events are also substantially different from those obtained for the HFA events. In helio current sheets, the increase of the ion kinetic crossover at the center of the sheet tends to be less dramatic compare to HFAs, and in some HCS events is completely missing. When the ion scale does increase, the enhancement was not well localized.

**Events 14 and 15** provide illustrative examples of such de-localized turbulent behavior. Event 14 detected on April 14, 2011 at  $\sim 20:29:00$  (Fig. 11, left) reveals the presence of ion-kinetic crossover (at  $\tau_i \sim 0.3 - 0.4$  s) both long before and after the current sheet crossing, the type of behavior that HFA events usually do not show. There is a rather short transient increases of the ion scale value to about 1.2 s after which the scalogram returns to its background state. A more consistent increase of  $\tau_i$  is observed during the passage of the trailing edge of event 14, with the upper range of ion kinetic scaling reaching 2 s. The blue-color coded gap which is present in the post-sector scalogram reveals a distorted shape of the structure function at the intermediate scales. The non-power law scaling associated with this gap could be a manifestation of a strong coherent oscillation inside the core region and the post-sector of the event. Polarization parameters of the oscillation are consistent with an obliquely propagating electromagnetic ion-cyclotron wave which could be excited by a two-stream instability caused by reflected solar wind ions.

Event 15 observed on May 06, 2011 at around 17:25:30 (Fig. 11, right) demonstrates a minor ion heating (from  $\sim 25$  to  $\sim 45$  eV) at the leading edge of the event, according to the shape of the SF scalogram. A similar transient temperature increase took place in the middle of the pre-sector of this HCS event showing that the heating was not limited to the interior of the current sheet. The  $\tau_i$  enhancement during this event is more evident than that during event 14, but its spatial domain is poorly defined.

**Event 17** (Fig. 12, left) was detected on July 13 2011 at about 00:46:30. Two distinct magnetic depression regions possibly associated with embedded current sheets have been recorded during this event. Spatial orienta-

tion of the magnetic field remained approximately constant before and after the event. During the passage of the core region, the B-field rotation angle reaches  $\sim 140$  degrees signaling strong directional discontinuity. The SF scalogram exhibits an increase of the ion kinetic time scale which is relatively well localized, with  $\tau_i$  reaching its highest value ( $\sim 0.8 - 1.0$  s) by the end of the event.

**Event 19** (Fig. 12, right) was encountered at about 00:46:30 on August 13 2011. The scalogram of this event reveals a rather hot plasma medium both in the core region and in the pre-sector for the event. This event shows a substantial change in the B-field direction and a fairly stable magnetic field orientation in the surrounding spatial domain.

The trailing boundaries of the core regions of events 17 and 19 carry significant plasma discontinuities associated with abrupt changes of the magnetic intensity by about 7-8 nT over a time interval 0.8-1.0 s. These B-field jumps correspond to a distance scale of the order of 400 km, assuming  $V_{SW} = 450$  km/s. The proton Larmor radius characterizing these structures is about 80 km according to the eq. 16 estimate. The discussed discontinuities are likely to have a kinetic origin while the large-scale HCS configuration seems to be formed in the MHD domain.

The rest of the HCS events identified by our code (see Table 2) feature similar sets of signatures. Compared to HFAs, these events tend to occur at a more significant upstream distance from the nominal bow shock, with  $d_B$  varying from 1.2 to 4.5  $R_M$ . They feature a larger B-field rotation angle accompanied by a smaller relative change of the field magnitude indicative of rotational discontinuities (see *Schwartz et al.* [2000] and references therein), a weaker magnetic connection with the bow shock as suggested by the local shock geometry which is often quasi-perpendicular (especially after the events), and a considerably more stable B-field orientation in the pre- and post-sectors. The SF scalogram analysis of the HCS events reveals broader spatial regions occupied by the heated plasma contrasting with more compact and spatially localized heating during HFA events.

## 5. Statistical survey

### 5.1. Event locations

Fig. 13 presents MSO positions of all the detected events classified into several groups. Black dots ( $n = 1337$ ) show automatically detected magnetic depression events satisfying the condition (2) with  $B_{th} = 5$  nT. Yellow crosses ( $n = 100$ ) show filtered events which, in addition to the threshold condition, met a set of criteria making them candidate HFAs. These events had the correct (toward) orientation of the motional electric field on at least one side ( $\theta_{E1:CS} \in [20, 70]$  and/or  $\theta_{E2:CS} \in [110, 160]$ ), the duration  $T$  of the core region between 10 and 100 s, and the distance  $d_{BS}$  to the model bow shock lying between -0.5 and 3.0  $R_M$ , with the negative (positive)  $d_{BS}$  values corresponding to the event positions inside (outside) of the model bow shock boundary.

Red symbols of different pattern designate the subset of the ten manually selected HFA-like events discussed in detail in the previous section. These events exhibit more reliable magnetic signatures of hot flow anomalies verified using a visual inspection and manual post-processing. The manually selected HFAs demonstrate identifiable compression edges on one or both sides of the event, a nearly perpendicular mutual orientation of  $\mathbf{n}_{CS}$  and  $\mathbf{n}_{BS}$  normals, and a consistently reduced B-field in the core region relative to the ambient pre- and post-

sectors ensuring  $\Delta B_0 > 0.5$ . As discussed earlier in the text, the fluctuation signatures of these events are suggestive of an ongoing ion heating not expected for foreshock cavities.

Blue symbols are used for the set of nine HCS events discussed earlier in the text which mimic the geometry and large-scale magnetic signatures of the HFAs but lack the compressed edges and turbulent signatures of kinetically active current sheets providing local plasma heating.

The first two planetary years of orbital MESSENGER operation covered a substantial portion of the dawn and dusk portions of the Hermean foreshock. The occurrence probability of all types of detected events is systematically higher in the dawn sector, which is in an agreement with terrestrial studies. It is known that on average, the dawn foreshock has a quasi-parallel magnetic field orientation allowing the reflected ions to be channeled onto the discontinuity. The post-midnight region characterized by large cone angles between the helio current sheets and the anti-sunward direction is of particular interest as it provides enough time for the kinetic processes to develop [Schwartz *et al.*, 2000]. A similar region at Earth is a preferred location of HFAs and a variety of other intermittent foreshock phenomena [Tsurutani and Stone, 1985].

The automatically detected population of magnetic depression events at Mercury shown by black dots in Fig. 13 may include a wide scope of activity not limited to HFA, in particular density holes – subminute events sharing many properties of early stage HFAs [Parks *et al.*, 2006; Wilber *et al.*, 2008], foreshock cavities – transient decreases of magnetic field strength and thermal ion density bounded by HFA-like edges of enhanced B-field [Billingham *et al.*, 2008], and SLAMS growing out of the ULF wave field and featuring nonconvective electric fields at the edges [Schwartz *et al.*, 1992]. In its turn, the filtered subset of events (yellow crosses) may, in principle, contain a fraction of HFA or proto-HFA events although their HFA-like properties can not be established with certainty. The requirement of the inwardly directed motional electric field on one or both sides removes from our statistics most of the density holes which tend to show an opposite (outward) E-field orientation. The prolonged duration of the filtered events is not characteristic, albeit not impossible, for the SLAMS events observed in the terrestrial foreshock [Schwartz *et al.*, 1992].

As has been already noted, most of the manually validated HFA events (except for event 1) are located just outside of the nominal bow shock boundary (Fig. 13, see also Table 1) while HCS events are observed systematically farther upstream. At Earth, hot flow anomalies are also formed when an interplanetary discontinuity with convergent motional electric field comes into direct contact with a quasi-parallel bow shock (within  $\pm 20\%$  from the model bow shock scaled by the observed solar wind dynamic pressure [Paschmann *et al.*, 1988]). HFAs passages are known to induce a significant magnetosheath response [Safrankova *et al.*, 2000; Sibeck *et al.*, 1999] allowing the magnetopause to move outward  $\sim 5$  planetary radii beyond its nominal position [Sibeck *et al.*, 1999] and causing significant effects in polar magnetosphere (see e.g. Eastwood *et al.* [2011]). Considering the proximity of the HFAs observed here to the bow shock boundary, one can expect that these events play an equally important role in Mercury’s magnetosphere.

## 5.2. Event parameters

Fig. 14 presents several types of ensemble-based statistics of the detected events.

980 Panel 14(a) shows the dependence between the pre-  
 981 sector and post-sector E-field angle with the current sheet  
 982 normal; panel 14(b) demonstrates a similar dependence  
 983 for the bow shock normal angles with the magnetic field.  
 984 Both panels use the same symbol notation as in Fig. 13.

985 It can be seen that the majority of the unfiltered  
 986 magnetic field depression events lie near the diagonal  
 987 line  $\theta_{E1:CS} = \theta_{E2:CS}$  corresponding to a constant mo-  
 988 tional electric field direction across the current sheet. For  
 989  $\theta_{E1:CS} < 90^\circ$ , the electric field is pointed toward the cur-  
 990 rent sheet in the pre-sector, which causes the solar wind  
 991 ions that are reflected by the bow shock immediately be-  
 992 fore the event to gyrate toward the current sheet. The  
 993 condition  $\theta_{E2:CS} > 90^\circ$  ensures similar behavior of the re-  
 994 flected particles at the trailing edge of the event. When  
 995 the convection E-field points toward the discontinuity on  
 996 both sides, the trajectories of the reflected ions from ei-  
 997 ther side converge on the sheet and become channeled  
 998 along it, see e.g. *Burgess* [1989]; *Schwartz* [1995]. This  
 999 configuration leading to the most efficient particle heat-  
 1000 ing corresponds to the upper left corner of the plot. Eight  
 1001 out of ten events with definite HFA signatures are located  
 1002 in this quadrant.

1003 Panel Fig.14(b) reveals no systematic tendency for the  
 1004 bow shock to become more quasi-perpendicular after the  
 1005 passage of automatically detected active current sheets.  
 1006 This tendency characterizes the behavior of Earth’s bow  
 1007 shock before and after HFA events [*Schwartz et al.*, 2000].  
 1008 Most of the HFA events validated manually, most notice-  
 1009 ably events 1, 5, 6 and 8, seem to violate this rule mak-  
 1010 ing the trailing edge bow shock more quasi-parallel. It  
 1011 remains to be understood whether these exceptions rep-  
 1012 resent a distinct physical tendency characteristic of HFAs  
 1013 at Mercury, or are caused by a statistical uncertainty.

1014 The probability distributions of the angles between the  
 1015 pre- and post-sector magnetic field shown in Fig. 14 (c)  
 1016 demonstrate significant differences. The automatically  
 1017 detected events, filtered and non-filtered, have a strong  
 1018 peak near  $\theta_{B1:B2} \sim 0$  consistent with the fact that mo-  
 1019 tional electric field remains unchanged across most of  
 1020 these events (since  $\mathbf{V}_{SW}$  is kept constant). The man-  
 1021 ually selected HFA events show a systematically stronger  
 1022 B-field rotation peaking at 30-90 degrees which is in a  
 1023 good agreement with the statistics of terrestrial HFAs  
 1024 showing a maximum occurrence rate at 40–90° [*Schwartz*  
 1025 *et al.*, 2000]. This is also consistent with the scattering  
 1026 the discontinuity angles describing interplanetary tangen-  
 1027 tial discontinuities found at 0.46 to 0.5 AU [*Lepping and*  
 1028 *Behannon*, 1986]. The population of HCS events shows  
 1029 an even stronger magnetic rotation with the maximum  
 1030 occurrence rate at 90 - 150 degrees.

1031 The distribution of the normalized change  $\Delta B_{12}$  of  
 1032 the field magnitude across the current sheets presented  
 1033 in Fig. 14(e) provides some additional insight into the na-  
 1034 ture of the underlying interplanetary discontinuities. For  
 1035 a “clean” TD,  $\Delta B_{12}$  is expected to be greater than 0.2,  
 1036 while smaller values correspond to mixed cases of either  
 1037 rotational or tangential discontinuity, depending on the  
 1038 normal magnetic field component. The  $\Delta B_{12}$  histogram  
 1039 makes it clear that more than a half of the automatically  
 1040 detected HFA-like events belong to the second (mixed)  
 1041 category. A similar fraction of hot flow anomalies at  
 1042 Earth [*Schwartz et al.*, 2000] have this property. Consid-  
 1043 ering that over 60% of the “mixed” cases may in fact also  
 1044 represent TDs [*Neugebauer et al.*, 1984], the total num-  
 1045 ber of tangential discontinuities in our database should  
 1046 dominate. This is important because our calculations  
 1047 of the current sheet normal is based on the assumption  
 1048 that the current sheets are TDs with a near-zero normal

1049 magnetic field component. This assumption is broadly  
 1050 used in single-spacecraft HFA studies. A more accurate  
 1051 identification of  $\mathbf{n}_{BS}$  would require a minimum variance  
 1052 analysis through the current sheet which cannot be im-  
 1053 plemented in the presence of the embedded HFAs.

1054 The probability distribution of  $\theta_{CS:BS}$  angles is biased  
 1055 toward large acute angles corresponding to perpendicu-  
 1056 lar orientation of the current sheets relative to the local  
 1057 bow shock. It is similar to the corresponding distribu-  
 1058 tion of terrestrial HFA events (compare with Fig. 10  
 1059 of *Schwartz et al.* [2000]). The  $\theta_{CS:BS}$  angle needs to  
 1060 be close to  $90^\circ$  in order to keep transit velocity  $V_{tr}$  suf-  
 1061 ficiently small to promote HFA formation. At Earth,  
 1062 about 80% of the HFAs have acute  $\theta_{CS:BS}$  angles greater  
 1063 than  $60^\circ$ . Our analysis also yields a significant fraction  
 1064 ( $\sim 65\%$ ) of such events at Mercury. These events had an  
 1065 appropriate spatial orientation with respect to the bow  
 1066 shock which could contribute to their successful devel-  
 1067 opment into HFAs. This scenario is supported by the  
 1068 shape of the histogram of the normalized transit veloc-  
 1069 ity  $|V_{tr}/V_g|$  which was constructed by putting together  
 1070 pre- and post-sector measurements (Fig. 14(f)). The his-  
 1071 togram shows a prevailing occurrence rate (above 70%)  
 1072 of smaller-than-one velocity ratios, even though most of  
 1073 the events were observed away from the subsolar point  
 1074 providing optimal current sheet - bow shock intersection  
 1075 conditions. The manually validated HFA events have the  
 1076 highest occurrence frequency of smaller-than-unity veloc-  
 1077 ity ratios among the studied groups of events.

### 5.3. Hermean HFA sizes compared to other planets

1078 It presents a certain interest to compare the estimated  
 1079 sizes of typical and extreme HFA events at Mercury with  
 1080 the corresponding sizes of HFA events reported for Earth  
 1081 and Saturn.

1082 To derive characteristic linear sizes of Hermean HFA  
 1083 events, we multiplied the duration of the core region of  
 1084 each event by the nominal solar wind velocity of 450  
 1085 km/s, and applied the correction factor  $\cos(\theta_{SW:CS})$  ac-  
 1086 counting for the  $\mathbf{n}_{CS}$  misalignment with the solar wind  
 1087 flow. Event 7 whose duration was by an order of mag-  
 1088 nitude longer than the duration of other events was ex-  
 1089 cluded from the statistics and treated separately.

1090 The typical size of terrestrial HFAs were taken from a  
 1091 global statistical survey conducted by *Facko et al.* [2009].  
 1092 Two of their estimates were used: the one based on the  
 1093 Alfvén speed (method 1) and the one based on the speed  
 1094 of the TD and bow shock intersection calculated from *in*  
 1095 *situ* solar wind measurements (method 2).

1096 As an example of an extreme terrestrial HFA we choose  
 1097 an event reported by *Safrankova et al.* [2012] based on  
 1098 multi-spacecraft observations. This event had a rather  
 1099 significant size and caused a considerable magnetosphere  
 1100 deformation.

1101 The typical size of HFA events at Saturn was evalu-  
 1102 ated using the data reported by *Masters et al.* [2009]; the  
 1103 largest event described in their paper was considered as  
 1104 an extreme event. The Kronian HFA sizes were evaluated  
 1105 for a nominal solar wind velocity of 450 km/s taking into  
 1106 account spatial orientation of the current sheets.

1107 Fig. 15 presents the comparison of the event sizes at  
 1108 the three planets.

1109 As can be seen, the size of the typical HFA tends to  
 1110 increase with the size of the planet. The dependence  
 1111 is approximately linear. To the first approximation, the  
 1112 size of the HFA at Mercury, Earth and Saturn is of the  
 1113 order of one planetary radius. The observed dependence  
 1114 can indicate that spatial dimensions of HFAs are con-

1115 trolled by the geometry of the bow shock, with the largest  
 1116 (Kronian) events formed at the least curved bow shock  
 1117 boundary.

1118 The data also show that the HFA size is directly pro-  
 1119 portional to the heliocentric distance (Fig. 15, bottom  
 1120 panel). This is an expected behavior since the sizes of  
 1121 the three compared planets scale approximately linearly  
 1122 with the distance from the Sun. The increase of the ion  
 1123 scales describing an expanding solar wind can contribute  
 1124 to the observed dependence. To illustrate this possibility,  
 1125 the figure provides characteristic values of proton inertial  
 1126 length and proton gyro radius calculated using the data-  
 1127 derived statistical solar wind model developed by [*Kohn-*  
 1128 *lein*, 1996]. It can be seen that both kinetic scales grow  
 1129 linearly with the heliocentric distance in proportion to  
 1130 the HFA size.

## 6. Concluding remarks

1131 We have presented first documented observations of  
 1132 HFA-like events at Mercury. Using magnetic and parti-  
 1133 cle data from MESSENGER collected over a course of  
 1134 two planetary years, we identified a representative en-  
 1135 semble of active current sheets magnetically connected to  
 1136 Mercury's bow shock. Some of these events exhibit un-  
 1137 ambiguous magnetic and particle signatures of hot flow  
 1138 anomalies. A broader subset of the detected magnetic  
 1139 depression events is likely to include a variety of plasma  
 1140 disturbances not limited to HFAs, such as the distur-  
 1141 bances associated with density holes, foreshock cavities,  
 1142 and SLAMS.

1143 Our classification of current sheets as HFAs is based on  
 1144 an investigation of the current sheet geometry involving  
 1145 all of the commonly used aspects such as the direction  
 1146 of the motional electric field, the bow shock location, the  
 1147 orientation of the current sheet and bow shock normals  
 1148 relative to the solar wind flow, and on a number of addi-  
 1149 tional tests. Four of the reported HFA events showed un-  
 1150 ambiguous signatures of ion energization documented by  
 1151 FIPS dynamic spectra confirming the presence of heated  
 1152 plasma inside and around the current sheets. Although  
 1153 accurate FIPS measurements have limited time resolu-  
 1154 tion and angular coverage, they provided a key piece of  
 1155 evidence by revealing hot plasma populations at the ex-  
 1156 pected locations.

1157 HFA events at Mercury are accompanied by a system-  
 1158 atic change in the magnetic turbulence spectrum pre-  
 1159 dicted for a locally energized solar wind plasma. Our pre-  
 1160 vious study [*Uritsky et al.*, 2011] has shown that the Her-  
 1161 mean magnetosphere, as well as the surrounding region,  
 1162 are affected by non-MHD effects introduced by finite sizes  
 1163 of cyclotron orbits of the constituting ion species. These  
 1164 results have demonstrated that plasma fluctuations at  
 1165 this planet are largely controlled by finite Larmor radius  
 1166 effects. The heating process associated with HFA-like ac-  
 1167 tive current sheets explored in the present paper are an  
 1168 important manifestation of such behavior at Mercury.

1169 One one occasion, we detected signatures of a ULF  
 1170 wave packet in a quasi-parallel shock configuration which  
 1171 was likely to be triggered by an HFA event. Such up-  
 1172 stream large-amplitude waves may propagate deep into  
 1173 Mercury's magnetosphere causing secondary instabilities  
 1174 in various plasma regions. They can also reach the sur-  
 1175 face through the thin atmosphere not protected by a con-  
 1176 ducting ionosphere.

1177 The occurrence rate of HFA events at Mercury is sys-  
 1178 tematically higher in the dawn sector compared to the  
 1179 dusk sector. On average, the dawn foreshock has a quasi-  
 1180 parallel magnetic field orientation allowing the reflected

ions to be channeled onto the discontinuity. A similar region at Earth is a preferred location of HFAs and a variety of other intermittent foreshock phenomena [Tsurutani and Stone, 1985]. The post-midnight region characterized by large cone angles between the helio current sheets and the anti-sunward direction is of particular interest as it provides enough time for the kinetic processes to develop. Most of our manually validated HFA events were encountered just outside of the nominal bow shock boundary. Because of their proximity to the bow shock boundary, such events can play an important role in Mercury’s magnetosphere. Terrestrial HFAs passages are known to induce a significant magnetosheath response [Safrankova et al., 2000; Sibeck et al., 1999] allowing the magnetopause to move outward  $\sim 5$  planetary radii beyond its nominal position and perturbing the magnetosphere (see e.g. Eastwood et al. [2011]). It would be important to verify in future studies whether similar global HFA-induced phenomena occur at Mercury. As an indirect manifestation of such behavior, there is a slight tendency for the bow shock to become more quasi-perpendicular after the passage of HFA-like events, which is also in line with the behavior of Earth’s bow shock before and after HFAs [Schwartz et al., 2000].

The characteristic linear size of HFA events at Mercury is noticeably smaller than that on other planets. When combined with previously reported HFA sizes at Earth and at Saturn, our measurements show that the size of planetary HFAs grows linearly with planetary radius. The observed dependence could reflect the bow shock geometry. An alternative explanation takes into account the fact that the size of the compared planets is proportional to their distance from the Sun. The increase in the heliocentric distance leads to larger ion scales in the expanding solar wind controlling the thickness of helio current sheets, and hence the size of the HFAs.

In summary, we have demonstrated that Mercury’s bow shock contains HFA events similar to those observed at other planets. The conducted quantitative analysis suggests that Mercury’s bow shock provides conditions for local particle acceleration and heating as predicted by previous numerical simulations. Together with earlier observations of HFA activity at Earth, Venus and Saturn, our results confirm that hot flow anomalies are a common property of planetary bow shocks.

**Acknowledgments.** The work of V.U. was supported by the NASA grant NNG11PL10A 670.002 through the CUAs Institute for Astrophysics and Computational Sciences.

## References

- 1229 Alexandrova, O., A. Mangeney, M. Maksimovic,  
1230 N. Cornilleau-Wehrin, J. M. Bosqued, and M. Andre  
1231 (2006), Alfvén vortex filaments observed in magnetosheath  
1232 downstream of a quasi-perpendicular bow shock, *J.*  
1233 *Geophysical Research – Space Phys.*, *111*(A12), A12,208,  
1234 doi:10.1029/2006JA011934.
- 1235 Alexandrova, O., V. Carbone, P. Veltri, and L. Sorriso-Valvo  
1236 (2008), Small-scale energy cascade of the solar wind turbu-  
1237 lence, *Astrophysical J.*, *674*(2), 1153–1157.
- 1238 Anderson, B. J., M. H. Acuna, D. A. Lohr, J. Scheifele,  
1239 A. Raval, H. Korth, and J. A. Slavin (2007), The Magne-  
1240 tometer instrument on MESSENGER, *Space Science Rev.*,  
1241 *131*(1-4), 417–450, doi:10.1007/s11214-007-9246-7.
- 1242 Anderson, B. J., M. H. Acuna, H. Korth, M. E. Purucker,  
1243 C. L. Johnson, J. A. Slavin, S. C. Solomon, and R. L.  
1244 McNutt (2008), The structure of Mercury’s magnetic field  
1245 from MESSENGER’s first flyby, *Science*, *321*(5885), 82–  
1246 85, doi:10.1126/science.1159081.
- 1247 Andrews, G. B., et al. (2007), The energetic particle and  
1248 plasma spectrometer instrument on the MESSENGER  
1249 spacecraft, *Space Science Rev.*, *131*(1-4), 523–556, doi:  
1250 10.1007/s11214-007-9272-5.
- 1251 Baker, D. N., et al. (2009), Space environment of mercury at  
1252 the time of the first MESSENGER flyby: Solar wind and  
1253 interplanetary magnetic field modeling of upstream condi-  
1254 tions, *J. Geophysical Research – Space Phys.*, *114*(A1),  
1255 A10101, doi:10.1029/2009JA014287.
- 1256 Billingham, L., S. J. Schwartz, and D. G. Sibeck (2008), The  
1257 statistics of foreshock cavities: results of a Cluster survey,  
1258 *Annales Geophysicae*, *26*(12), 3653–3667.
- 1259 Billingham, L., S. J. Schwartz, and M. Wilber (2011),  
1260 Foreshock cavities and internal foreshock bound-  
1261 aries, *Planetary Space Science*, *59*(7), 456–467, doi:  
1262 10.1016/j.pss.2010.01.012.
- 1263 Biskamp, D. (2003), *Magnetohydrodynamic turbulence*, Cam-  
1264 bridge Univ. Press.
- 1265 Boardsen, S. A., B. J. Anderson, M. H. Acuna, J. A. Slavin,  
1266 H. Korth, and S. C. Solomon (2009), Narrow-band ultra-  
1267 low-frequency wave observations by MESSENGER dur-  
1268 ing its January 2008 flyby through Mercury’s magneto-  
1269 sphere, *Geophysical Research Lett.*, *36*(1), L01,104, doi:  
1270 10.1029/2008GL036034.
- 1271 Burgess, D. (1989), On the effect of a tangential disconti-  
1272 nuity on ions specularly reflected at an oblique shock, *J.*  
1273 *Geophysical Research – Space Phys.*, *94*(A1), 472–478, doi:  
1274 10.1029/JA094iA01p00472.
- 1275 Collinson, G. A., L. B. Wilson, III, D. G. Sibeck,  
1276 N. Shane, T. L. Zhang, T. E. Moore, A. J. Coates, and  
1277 S. Barabash (2012), Short large-amplitude magnetic struc-  
1278 tures (SLAMS) at Venus, *J. Geophysical Research – Space*  
1279 *Phys.*, *117*(A16), A10221.
- 1280 Collinson, G. A., et al. (2012), Hot flow anomalies at Venus,  
1281 *J. Geophysical Research – Space Phys.*, *117*, A04,204, doi:  
1282 10.1029/2011JA017277.
- 1283 Eastwood, J. P., E. A. Lucek, C. Mazelle, K. Meziane,  
1284 Y. Narita, J. Pickett, and R. A. Treumann (2005),  
1285 The foreshock, *Space Science Rev.*, *118*(1-4), 41–94, doi:  
1286 10.1007/s11214-005-3824-3.
- 1287 Eastwood, J. P., T. D. Phan, S. D. Bale, and A. Tjulin  
1288 (2009), Observations of turbulence generated by mag-  
1289 netic reconnection, *Phys. Rev. Lett.*, *102*(3), 035,001, doi:  
1290 10.1103/PhysRevLett.102.035001.
- 1291 Eastwood, J. P., S. J. Schwartz, T. S. Horbury, C. M. Carr,  
1292 K. H. Glassmeier, I. Richter, C. Koenders, F. Plaschke, and  
1293 J. A. Wild (2011), Transient Pc3 wave activity generated  
1294 by a hot flow anomaly: Cluster, Rosetta, and ground-based  
1295 observations, *J. Geophysical Research – Space Phys.*, *116*,  
1296 A08,224, doi:10.1029/2011JA016467.
- 1297 Eastwood, J. P., et al. (2008), Themis observations of a hot  
1298 flow anomaly: Solar wind, magnetosheath, and ground-  
1299 based measurements, *Geophysical Research Lett.*, *35*(17),  
1300 L17S03, doi:10.1029/2008GL033475.
- 1301 Facsko, G., Z. Nemeth, G. Erdos, A. Kis, and I. Dandouras  
1302 (2009), A global study of hot flow anomalies using Clus-

- 1303 ter multi-spacecraft measurements, *Annales Geophysicae*,  
1304 27(5), 2057–2076.
- 1305 Kohnlein, W. (1996), Radial dependence of solar wind pa-  
1306 rameters in the ecliptic, *Solar Phys.*, 169(1), 209–213, doi:  
1307 10.1007/BF00153841.
- 1308 Korth, H., B. J. Anderson, T. H. Zurbuchen, J. A. Slavin,  
1309 S. Perri, S. A. Boardsen, D. N. Baker, S. C. Solomon,  
1310 and R. L. McNutt, Jr. (2010), The interplanetary magnetic  
1311 field environment at Mercury’s orbit, *Planetary Space Sci.*,  
1312 59(15), 2075–2085, doi:10.1016/j.pss.2010.10.014.
- 1313 Lepping, R. P., and K. W. Behannon (1986), Magnetic-field di-  
1314 rectional discontinuities - characteristics between 0.46 and  
1315 1.0 AU, *J. Geophysical Research – Space Phys.*, 91(A8),  
1316 8725–8741, doi:10.1029/JA091iA08p08725.
- 1317 Masters, A., et al. (2008), Cassini encounters with  
1318 hot flow anomaly-like phenomena at Saturn’s bow  
1319 shock, *Geophysical Research Lett.*, 35(2), L02,202, doi:  
1320 10.1029/2007GL032371.
- 1321 Masters, A., et al. (2009), Hot flow anomalies at Saturn’s  
1322 bow shock, *J. Geophysical Research – Space Phys.*, 114,  
1323 A08,217, doi:10.1029/2009JA014112.
- 1324 Matthaeus, W. H., and M. L. Goldstein (1982), Stationarity  
1325 of magnetohydrodynamic fluctuations in the solar wind, *J.*  
1326 *Geophysical Research – Space Phys.*, 87(NA12), 347–354.
- 1327 Matthaeus, W. H., S. Dasso, J. M. Weygand, L. J. Milano,  
1328 C. W. Smith, and M. G. Kivelson (2005), Spatial corre-  
1329 lation of solar-wind turbulence from two-point measure-  
1330 ments, *Phys. Rev. Lett.*, 95(23), 231,101.
- 1331 Monin, A. S., and A. M. Yaglom (1975), *Statistical fluid me-*  
1332 *chanics: Mechanics of turbulence*, vol. Vol. 2, MIT Press.
- 1333 Neugebauer, M., D. R. Clay, B. E. Goldstein, B. T. Tsuru-  
1334 tani, and R. D. Zwickl (1984), A reexamination of rota-  
1335 tional and tangential discontinuities in the solar wind, *J.*  
1336 *Geophysical Research – Space Phys.*, 89(NA7), 5395–5408,  
1337 doi:10.1029/JA089iA07p05395.
- 1338 Øieroset, M., D. L. Mitchell, T. D. Phan, R. P. Lin, and  
1339 M. H. Acuna (2001), Hot diamagnetic cavities upstream of  
1340 the Martian bow shock, *Geophysical Research Lett.*, 28(5),  
1341 887–890, doi:10.1029/2000GL012289.
- 1342 Omid, N., and D. G. Sibeck (2007), Formation of  
1343 hot flow anomalies and solitary shocks, *J. Geophys-*  
1344 *ical Research – Space Phys.*, 112(A1), A01,203, doi:  
1345 10.1029/2006JA011663.
- 1346 Parks, G. K., et al. (2006), Larmor radius size density holes  
1347 discovered in the solar wind upstream of Earth’s bow shock,  
1348 *Phys. Plasmas*, 13(5), 050,701, doi:10.1063/1.2201056.
- 1349 Paschmann, G., G. Haerendel, N. Sckopke, E. Mobius,  
1350 H. Luhr, and C. W. Carlson (1988), 3-dimensional plasma  
1351 structures with anomalous flow directions near the Earth’s  
1352 bow shock, *J. Geophysical Research – Space Phys.*,  
1353 93(A10), 11,279–11,294, doi:10.1029/JA093iA10p11279.
- 1354 Raines, J. M., J. A. Slavin, T. H. Zurbuchen, G. Gloeckler,  
1355 B. J. Anderson, D. N. Baker, H. Korth, S. M. Krimigis,  
1356 and R. L. McNutt, Jr (2011), MESSENGER observations  
1357 of the plasma environment near Mercury, *Planetary Space*  
1358 *Sci.*, 59(15), 2004–2015, doi:10.1016/j.pss.2011.02.004.
- 1359 Safrankova, J., L. Prech, Z. Nemecek, D. G. Sibeck, and  
1360 T. Mukai (2000), Magnetosheath response to the interplan-  
1361 etary magnetic field tangential discontinuity, *J. Geophys-*  
1362 *ical Research – Space Phys.*, 105(A11), 25,113–25,121, doi:  
1363 10.1029/1999JA000435.
- 1364 Safrankova, J., O. Goncharov, Z. Nemecek, L. Prech, and  
1365 D. G. Sibeck (2012), Asymmetric magnetosphere deformation  
1366 driven by hot flow anomaly(ies), *Geophysical Research*  
1367 *Lett.*, 39, L15,107, doi:10.1029/2012GL052636.
- 1368 Sahraoui, F., M. L. Goldstein, P. Robert, and Y. V. Khotyaint-  
1369 sev (2009), Evidence of a cascade and dissipation of solar-  
1370 wind turbulence at the electron gyroscale, *Phys. Rev. Lett.*,  
1371 102(23), 231,102, doi:10.1103/PhysRevLett.102.231102.
- 1372 Savin, S., et al. (2012), Super fast plasma streams as drivers  
1373 of transient and anomalous magnetospheric dynamics, *An-*  
1374 *nales Geophysicae*, 30(1), 1–7, doi:10.5194/angeo-30-1-  
1375 2012.
- 1376 Schekochihin, A. A., S. C. Cowley, and W. Dorland  
1377 (2007), Interplanetary and interstellar plasma turbulence,  
1378 *Plasma Phys. Controlled Fusion*, 49(5A), A195–A209, doi:  
1379 10.1088/0741-3335/49/5A/S16.

- 1380 Schwartz, S. J. (1995), Hot flow anomalies near the Earth's  
1381 bow shock, *Adv. Space Res.*, *15*(8-9), 107–116, doi:  
1382 10.1016/0273-1177(94)00092-F.
- 1383 Schwartz, S. J., M. F. Thomsen, and J. T. Gosling (1983),  
1384 Ions upstream of the earth's bow shock - a theoretical  
1385 comparison of alternative source populations, *J. Geophys-  
1386 ical Research - Space Phys.*, *88*(NA3), 2039–2047, doi:  
1387 10.1029/JA088iA03p02039.
- 1388 Schwartz, S. J., D. Burgess, W. P. Wilkinson, R. L. Kessel,  
1389 M. Dunlop, and H. Luhr (1992), Observations of short  
1390 large-amplitude magnetic-structures at a quasi-parallel  
1391 shock, *J. Geophysical Research - Space Phys.*, *97*(A4),  
1392 4209–4227, doi:10.
- 1393 Schwartz, S. J., G. Paschmann, N. Sckopke, T. M. Bauer,  
1394 M. Dunlop, A. N. Fazakerley, and M. F. Thomsen (2000),  
1395 Conditions for the formation of hot flow anomalies at  
1396 Earth's bow shock, *J. Geophysical Research - Space Phys.*,  
1397 *105*(A6), 12,639–12,650, doi:10.1029/1999JA000320.
- 1398 Schwartz, S. J., et al. (1985), An active current sheet  
1399 in the solar-wind, *Nature*, *318*(6043), 269–271, doi:  
1400 10.1038/318269a0.
- 1401 Sibeck, D. G., et al. (1999), Comprehensive study of the  
1402 magnetospheric response to a hot flow anomaly, *J. Geo-  
1403 physical Research - Space Phys.*, *104*(A3), 4577–4593, doi:  
1404 10.1029/1998JA900021.
- 1405 Singh, N., G. Khazanov, and A. Mukhter (2007), Electro-  
1406 static wave generation and transverse ion acceleration by  
1407 Alfvénic wave components of broadband extremely low fre-  
1408 quency turbulence, *J. Geophysical Research - Space Phys.*,  
1409 *112*(A6), A06,210, doi:10.1029/2006JA011933.
- 1410 Slavin, J. A., et al. (2008), Mercury's magnetosphere after  
1411 MESSENGER's first flyby, *Science*, pp. 85–89.
- 1412 Slavin, J. A., et al. (2009a), MESSENGER observa-  
1413 tions of Mercury's magnetosphere during northward  
1414 IMF, *Geophysical Research Lett.*, *36*, L02101, doi:  
1415 10.1029/2008GL036158.
- 1416 Slavin, J. A., et al. (2009b), MESSENGER and Venus  
1417 Express observations of the solar wind interaction with  
1418 Venus, *Geophysical Research Lett.*, *36*, L09,106, doi:  
1419 10.1029/2009GL037876.
- 1420 Slavin, J. A., et al. (2009c), Messenger observations of mag-  
1421 netic reconnection in Mercury's magnetosphere, *Science*,  
1422 *324*(5927), 606–610, doi:10.1126/science.1172011.
- 1423 Slavin, J. A., et al. (2010), MESSENGER observations of large  
1424 flux transfer events at Mercury, *Geophysical Research Lett.*,  
1425 *37*, L02,105, doi:10.1029/2009GL041485.
- 1426 Solomon, S. C., et al. (2001), The MESSENGER mission to  
1427 Mercury: scientific objectives and implementation, *Plane-  
1428 tary Space Science*, *49*(14-15), 1445–1465.
- 1429 Sundberg, T., S. A. Boardsen, J. A. Slavin, L. G. Blomberg,  
1430 and H. Korth (2010), The Kelvin-Helmholtz instability at  
1431 Mercury: an assessment, *Planetary Space Science*, *58*(11),  
1432 1434–1441, doi:10.1016/j.pss.2010.06.008.
- 1433 Sundberg, T., et al. (2012), MESSENGER observations of  
1434 dipolarization events in Mercury's magnetotail, *J. Geo-  
1435 physical Research - Space Phys.*, *117*, A00M03, doi:  
1436 10.1029/2012JA017756.
- 1437 Thomsen, M. F., J. T. Gosling, S. A. Fuselier, S. J. Bame, and  
1438 C. T. Russell (1986), Hot, diamagnetic cavities upstream  
1439 from the earth's bow shock, *J. Geophysical Research - Space  
1440 Phys.*, *91*(A3), 2961–2973, doi:10.1029/JA091iA03p02961.
- 1441 Thomsen, M. F., J. T. Gosling, S. J. Bame, K. B. Quest,  
1442 C. T. Russell, and S. A. Fuselier (1988), On the origin  
1443 of hot diamagnetic cavities near the Earth's bow shock,  
1444 *J. Geophysical Research - Space Phys.*, *93*(A10), 11,311–  
1445 11,325, doi:10.1029/JA093iA10p11311.
- 1446 Thomsen, M. F., V. A. Thomas, D. Winske, J. T. Gosling,  
1447 M. H. Farris, and C. T. Russell (1993), Observational test  
1448 of hot flow anomaly formation by the interaction of a  
1449 magnetic discontinuity with the bow shock, *J. Geophys-  
1450 ical Research - Space Phys.*, *98*(A9), 15,319–15,330, doi:  
1451 10.1029/93JA00792.
- 1452 Tjulin, A., E. A. Lucek, and I. Dandouras (2008), Wave  
1453 activity inside hot flow anomaly cavities, *J. Geophys-  
1454 ical Research - Space Phys.*, *113*(A8), A08,113, doi:  
1455 10.1029/2008JA013333.

- 1456 Tsurutani, B. T., and R. G. Stone (Eds.) (1985), *Collisionless*  
1457 *shocks in the heliosphere: reviews of current research*, *Geo-*  
1458 *physical Monograph*, vol. 35, American Geophysical Union.
- 1459 Uritsky, V. M., J. A. Slavin, G. V. Khazanov, E. F. Dono-  
1460 van, S. A. Boardsen, B. J. Anderson, and H. Korth (2011),  
1461 Kinetic-scale magnetic turbulence and finite Larmor radius  
1462 effects at Mercury, *J. Geophysical Research – Space Phys.*,  
1463 *116*, A09,236.
- 1464 Wilber, M., G. K. Parks, K. Meziane, N. Lin, E. Lee,  
1465 C. Mazelle, and A. Harris (2008), Foreshock density holes  
1466 in the context of known upstream plasma structures, *An-*  
1467 *nales Geophysicae*, *26*(12), 3741–3755.
- 1468 Yordanova, E., A. Vaivads, M. Andre, S. C. Buchert, and  
1469 Z. Vörös (2008), Magnetosheath plasma turbulence and its  
1470 spatiotemporal evolution as observed by the Cluster space-  
1471 craft, *Phys. Rev. Lett.*, *100*(205003), 205,003–1 – 4.

---

1472 V. M. Uritsky, Catholic University of America at NASA  
1473 Goddard Space Flight Center, Code 671, Greenbelt, MD  
1474 20771, USA. (vadim.uritsky@nasa.gov)

**Table 1.** Parameters of HFA-like events

Event	1	2	3	4	5	6	7	8	9	10
mm/dd	04/16	04/16	04/20	04/21	05/04	05/04	05/07	08/13	08/13	08/13
$\frac{(t'_0 + t''_0)}{2}$	19:00:20	19:09:10	04:50:44	03:52:52	06:08:30	18:26:42	04:46:02	04:28:04	04:29:12	02:22:48
$X_{MS0}$	-0.96	-0.86	1.58	2.20	-0.24	-0.26	-1.29	-3.08	-3.09	-2.13
$Y_{MS0}$	0.12	-0.01	-1.97	-3.55	-3.78	-3.47	-4.45	-2.42	-2.43	-1.23
$Z_{MS0}$	-4.50	-4.73	0.42	-1.77	-1.04	-0.58	-3.98	-5.70	-5.69	-6.65
$d_{BS}$	-0.56	-0.80	-0.50	-2.21	-0.52	-0.19	-1.60	-0.90	-0.88	-1.86
$\theta_{B1:B2}$	18	158	44	81	63	73	2	36	50	32
$\theta_{E1:CS}$	155	37	46	43	52	66	27	74	67	84
$\theta_{E2:CS}$	151	148	108	109	103	152	24	143	142	125
$\theta_{B1:BS}$	159	88	160	136	41	52	69	54	34	40
$\theta_{B2:BS}$	174	94	154	141	22	21	70	25	79	72
$\theta_{CS:BS}$	94	8	90	88	96	96	24	111	112	99
$\theta_{SW:CS}$	112	119	120	130	134	114	98	110	115	123
$\Delta B_{12}$	0.20	0.05	0.41	0.13	0.08	0.09	0.15	0.08	0.15	0.09
$\Delta B_0$	1.09	0.77	2.06	0.48	1.02	1.07	0.62	0.37	0.37	0.28
$\Delta t, s$	20	21	18	12	10	6	287	17	13	4
$ V_{tr}/V_g _1$	0.98	2.87	0.92	0.64	0.86	0.42	0.35	0.48	0.86	0.88
$ V_{tr}/V_g _2$	3.83	2.88	0.71	0.71	1.46	0.89	0.35	0.90	0.50	0.60

**Table 2.** Parameters of HCS events

Event	11	12	13	14	15	16	17	18	19
mm/dd	04/11	04/13	04/21	04/21	05/06	05/11	07/13	07/27	08/13
$\frac{(t'_0 + t''_0)}{2}$	19:12:18	11:30:20	03:13:34	20:29:00	17:25:30	04:11:09	00:46:29	23:24:28	01:12:30
$X_{MS0}$	-0.06	3.02	2.30	-0.55	-1.04	-2.20	2.91	-0.67	-1.37
$Y_{MS0}$	-0.74	-2.74	-3.92	-0.40	-4.41	-3.76	-2.87	0.56	-0.40
$Z_{MS0}$	-5.66	-5.81	-2.88	-5.49	-2.94	-5.27	-2.08	-5.04	-6.50
$d_{BS}$	-2.07	-4.54	-2.89	-1.62	-1.18	-1.57	-2.47	-1.20	-2.02
$\theta_{B1:B2}$	116	97	170	108	139	123	141	23	38
$\theta_{E1:CS}$	58	26	68	16	53	69	25	19	85
$\theta_{E2:CS}$	153	141	104	144	114	115	157	20	145
$\theta_{B1:BS}$	131	106	81	139	44	23	57	97	65
$\theta_{B2:BS}$	29	52	93	109	98	100	85	91	100
$\theta_{CS:BS}$	67	39	31	105	67	83	105	17	65
$\theta_{SW:CS}$	115	114	138	106	142	153	112	109	112
$\Delta B_{12}$	0.15	0.13	0.52	0.09	0.15	0.26	0.03	0.10	0.42
$\Delta B_0$	0.48	0.21	0.88	0.70	0.57	0.36	0.98	0.24	0.54
$\Delta t, s$	14	31	10	18	18	9	24	3	23
$ V_{tr}/V_g _1$	0.56	0.50	1.03	0.39	1.12	2.25	0.30	0.99	0.45
$ V_{tr}/V_g _2$	0.83	0.60	1.02	0.27	0.79	0.92	0.25	0.98	0.42

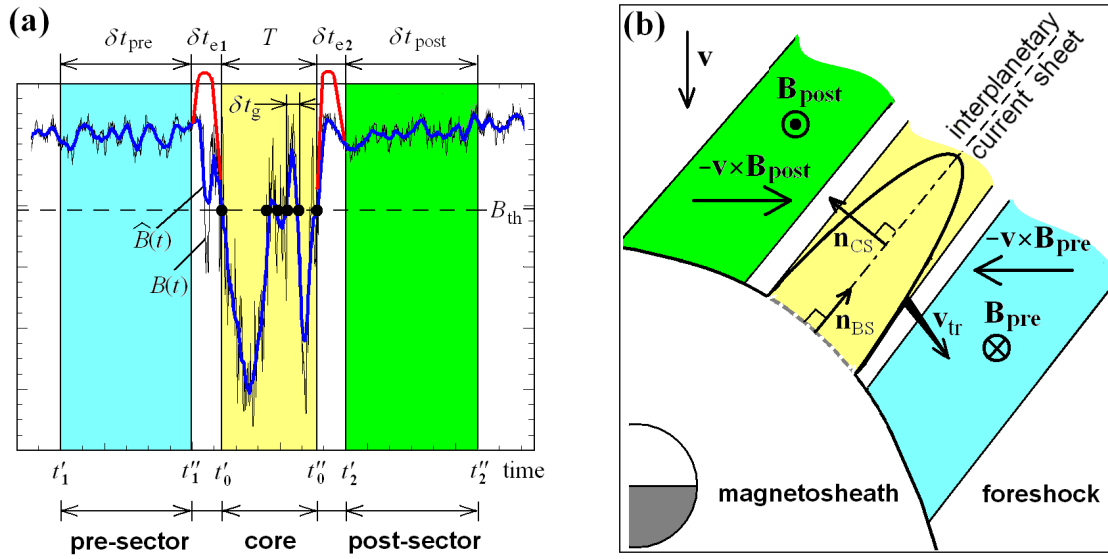


**Figure 1.** (a): Illustration of the threshold-based detection of an HFA event in the Hermean foreshock. (b): Spatial structure of the event. See text for details.

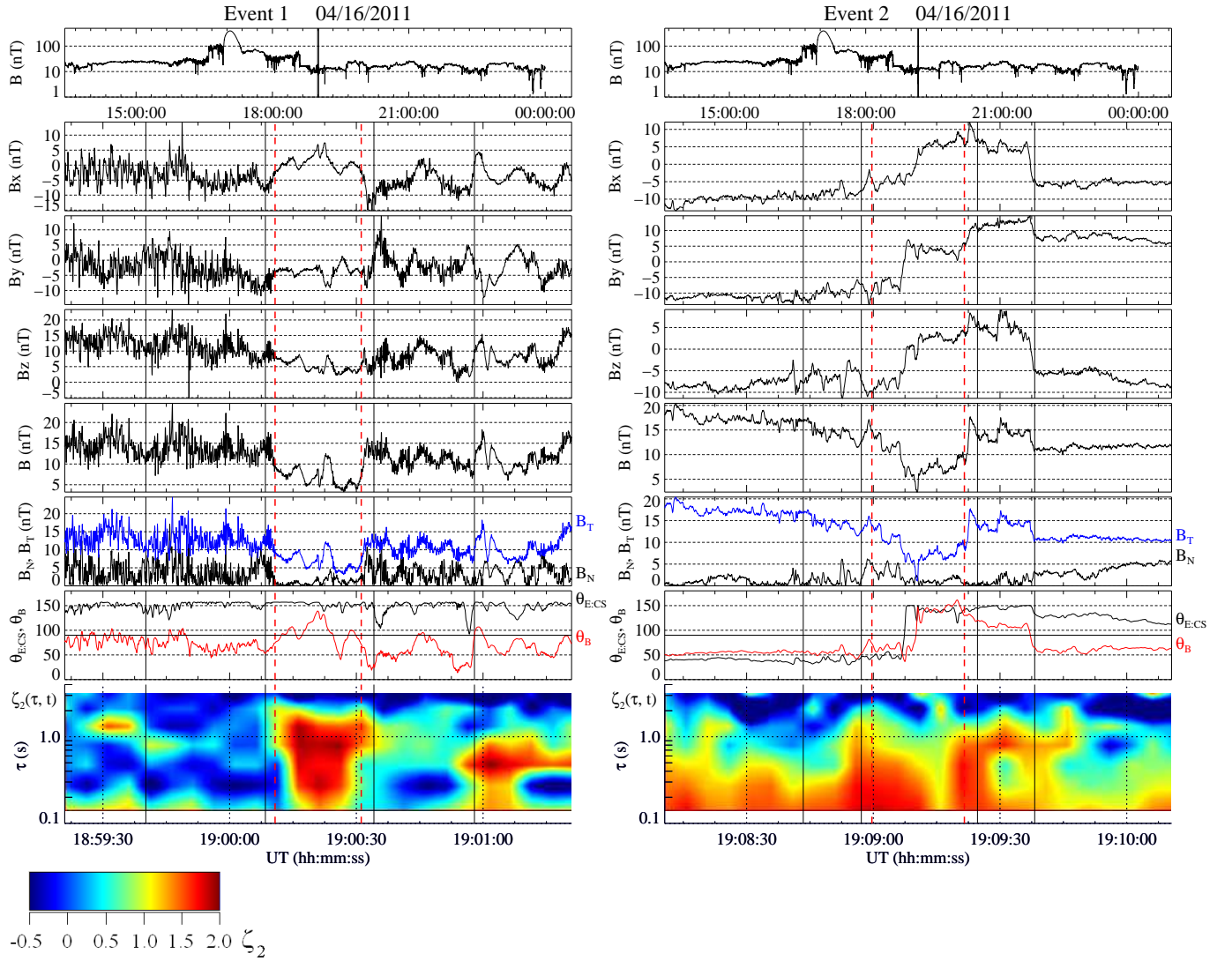


**Figure 2.** Magnetic and turbulent signatures of two hot flow anomaly events observed on April 16 2011. The top panels shows large-scale variations of the B-field magnitude  $B$ , with the black vertical line marking the timing of the event. The remaining panels (from top to bottom) show zoomed-in plots of the  $B_x$ ,  $B_y$  and  $B_z$  MSO magnetic field components; the B-field magnitude  $B$ ; the tangential ( $B_T$ ) and normal ( $B_N$ ) magnetic field components in the current sheet coordinate system determined using eq. (10); the angle  $\theta_{E:CS}$  (black line) between the motional E-field and the current sheet normal and the cone angle  $\theta_B$  (red line) between the magnetic field and the anti-sunward direction; the SF scalogram showing temporal evolution of the second-order structure function exponent  $\zeta_2$  estimated at different temporal scales  $\tau$ . The  $\zeta_2$  color coding is the same for all the scalogram plots presented in this paper. Red dashed vertical lines show the boundaries of the core region, black solid lines mark the pre- and post sectors of the event.

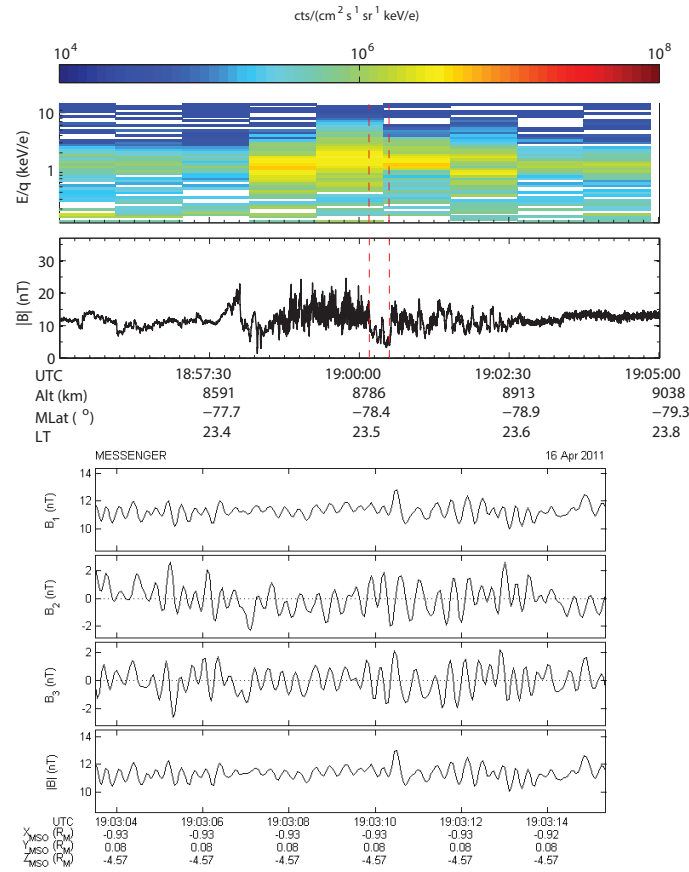


**Figure 3.** Top panel: Combined plots of FIPS and MAG observations of the hot flow anomaly event 1 shown in Fig. 2(left). The core region of the event is marked with red vertical lines. Bottom panel: left-hand polarized 3-4 Hz wave activity after the event. The right hand plot is given in field-aligned coordinates, where  $B_1$  is the direction of the mean field over the plotted interval, and  $B_2$  and  $B_3$  are the transverse components, with the corresponding unit vectors  $\mathbf{n}_1 = [-0.85, 0.51, 0.13]$ ,  $\mathbf{n}_2 = [0.52, 0.85, 0.00]$ , and  $\mathbf{n}_3 = [-0.11, 0.066, -0.99]$ .

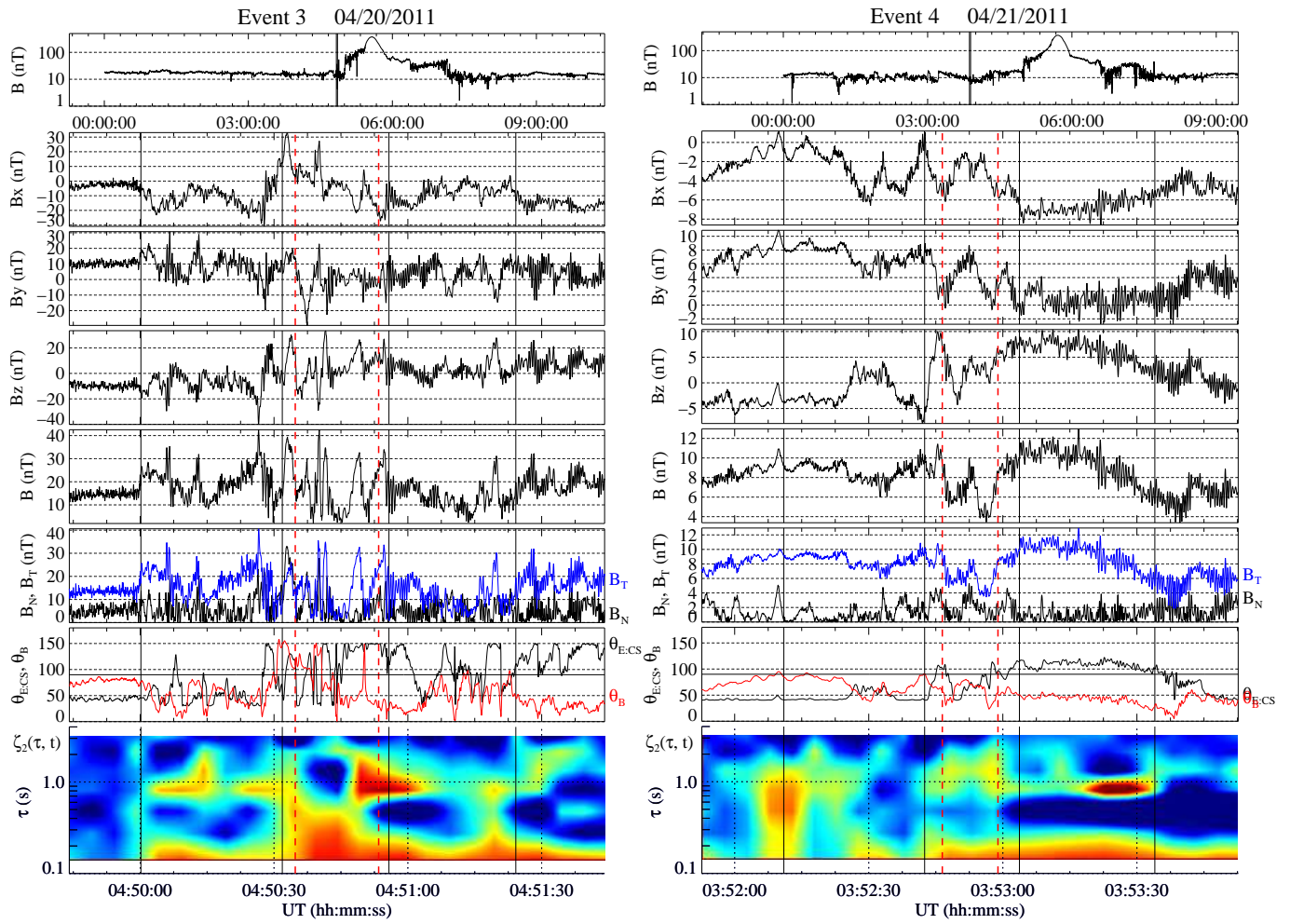


Figure 4. Hot flow anomalies observed on April 20 and April 21, 2011.

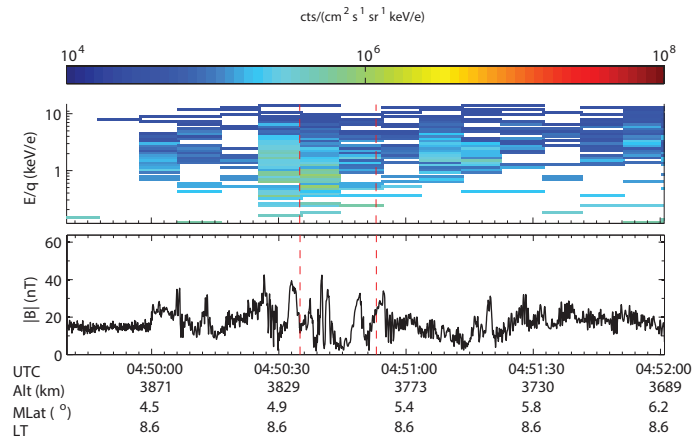


Figure 5. Combined plots of FIPS and MAG observations of the hot flow anomaly event 3 shown in Fig. 4(left). The core region of the event is marked with red vertical lines.

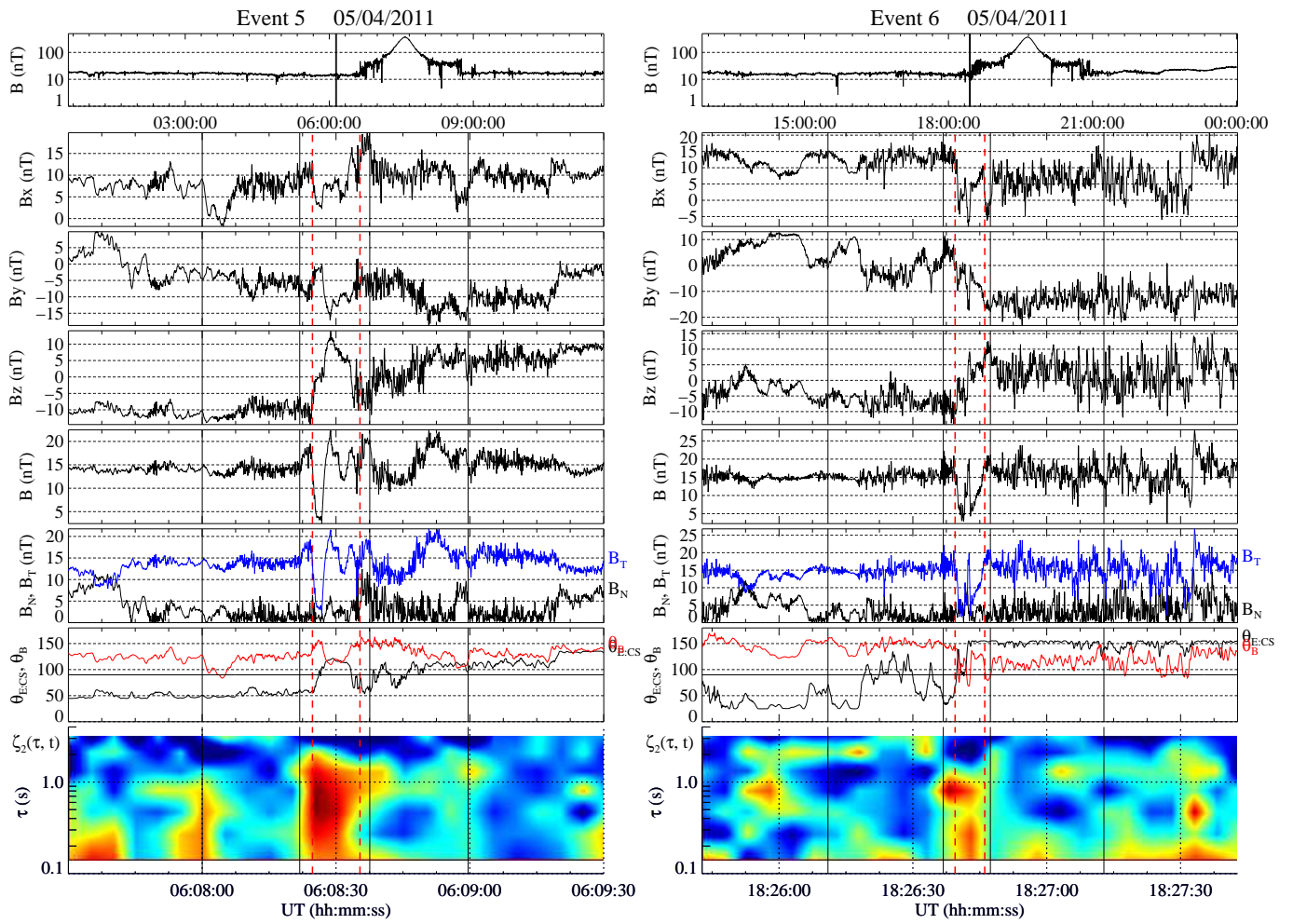


Figure 6. Hot flow anomalies observed on May 04, 2011.

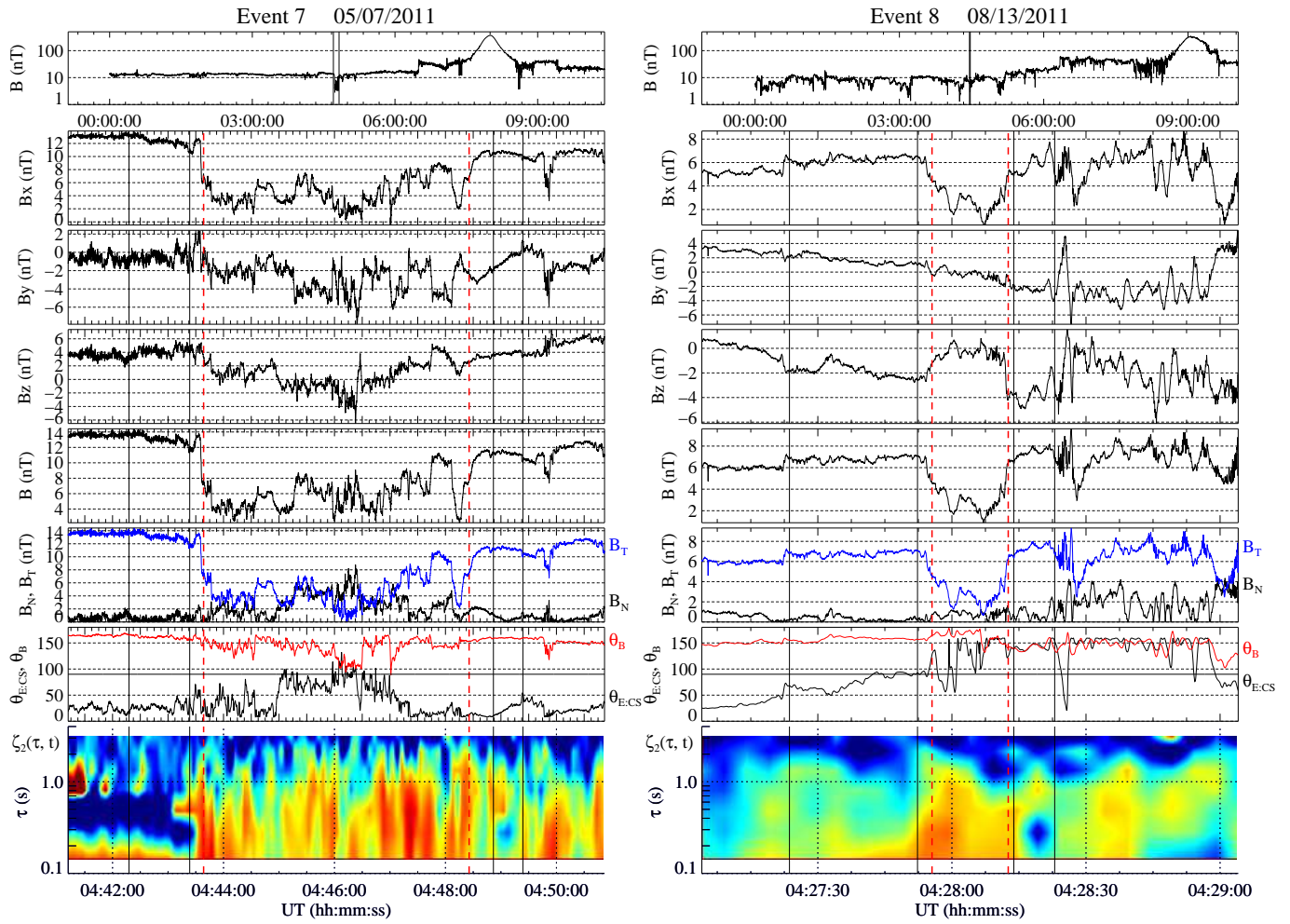


Figure 7. Hot flow anomaly - like events observed on May 07 and August 13, 2011.

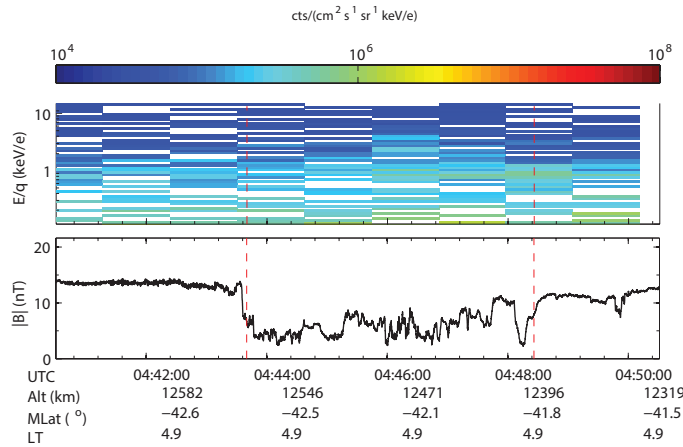
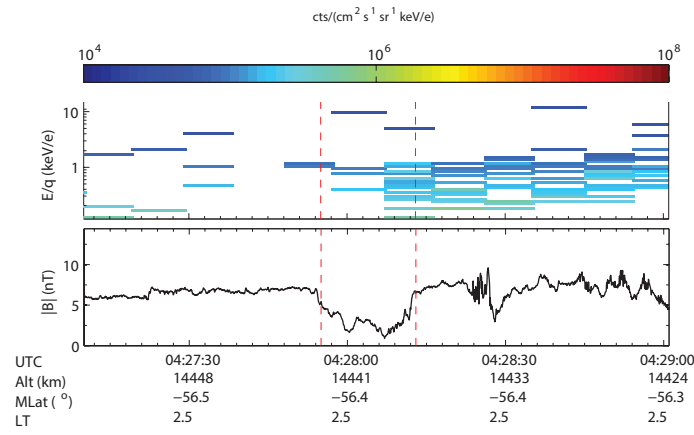
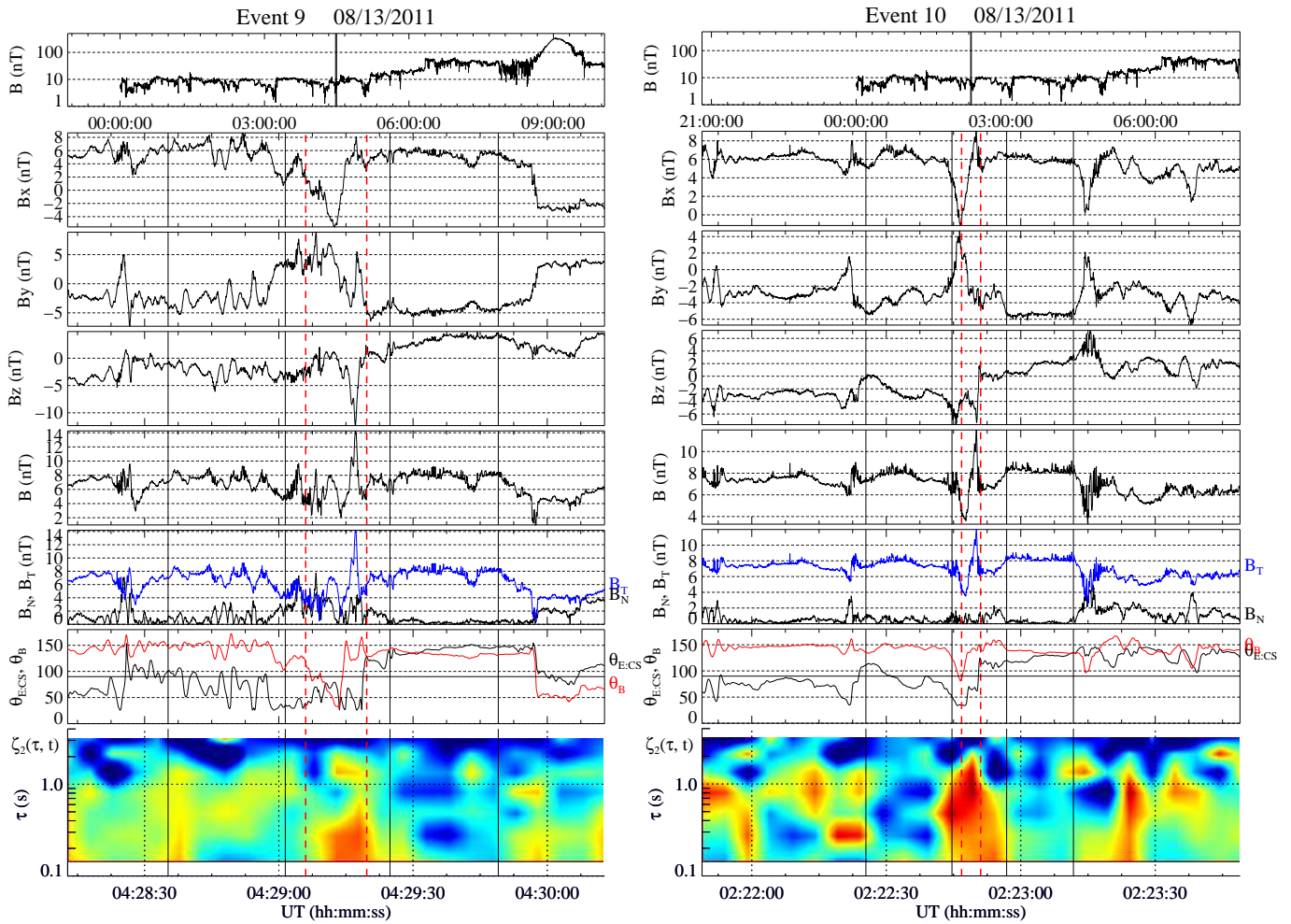


Figure 8. Combined plots of FIPS and MAG observations of the hot flow anomaly event 7 shown in Fig. 7 (left column). The core region of the event is marked with red vertical lines.



**Figure 9.** Combined plots of FIPS and MAG observations of the hot flow anomaly event 8 shown in Fig. 7 (right column). The core region of the event is marked with red vertical lines.



**Figure 10.** Two hot flow anomalies observed on Augusts 13, 2011.

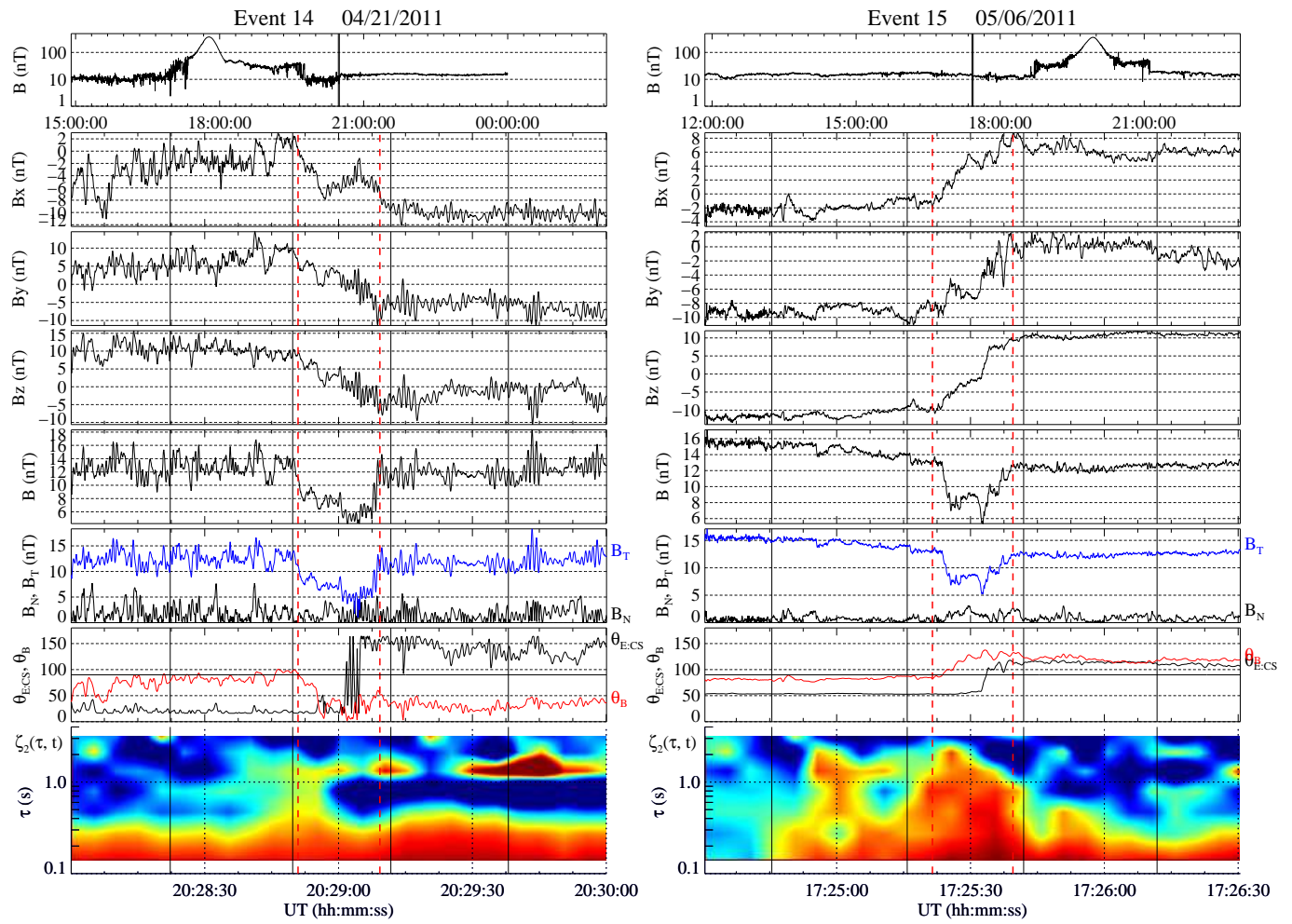


Figure 11. Examples of heliospheric current sheets in an upstream foreshock region.

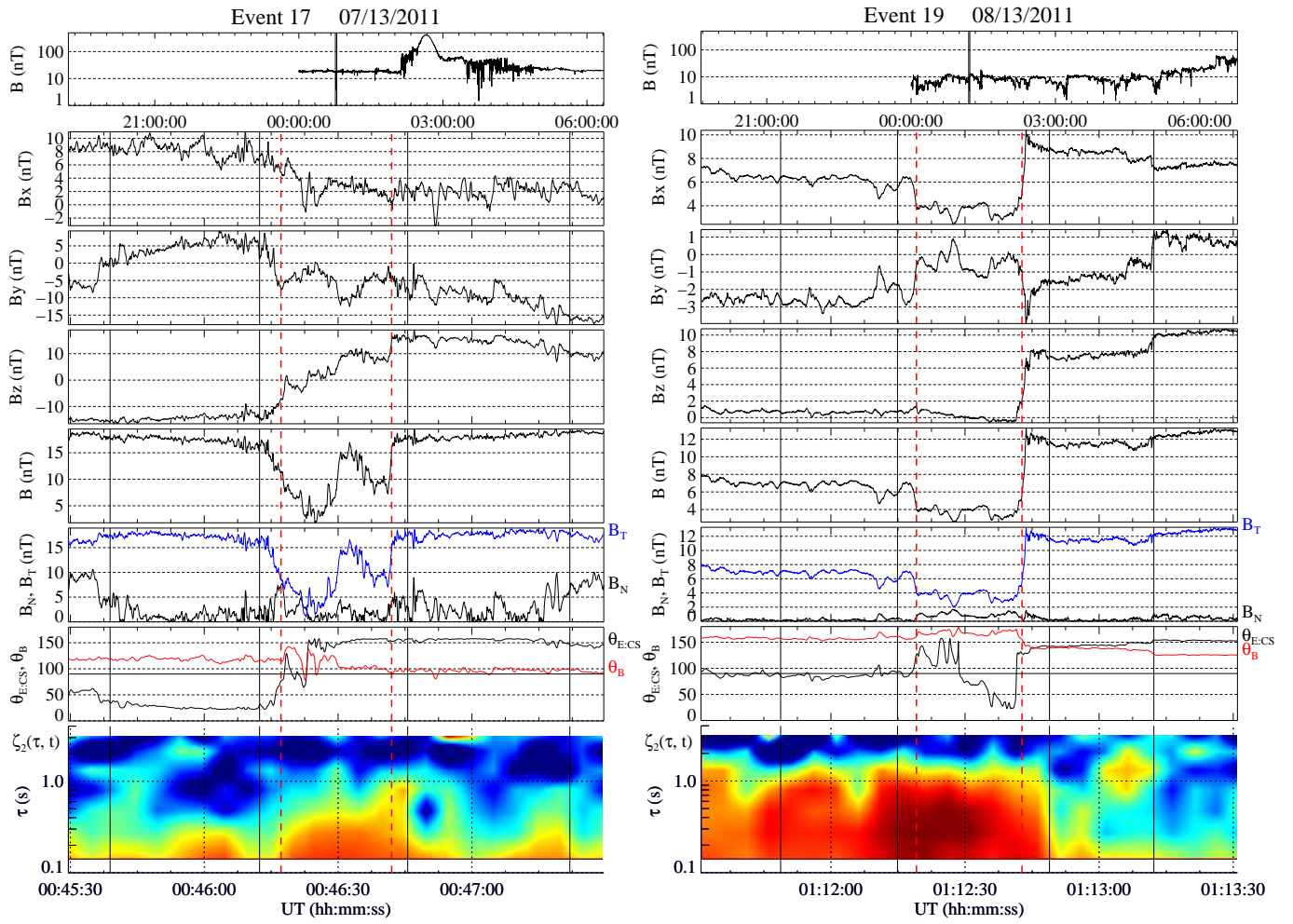
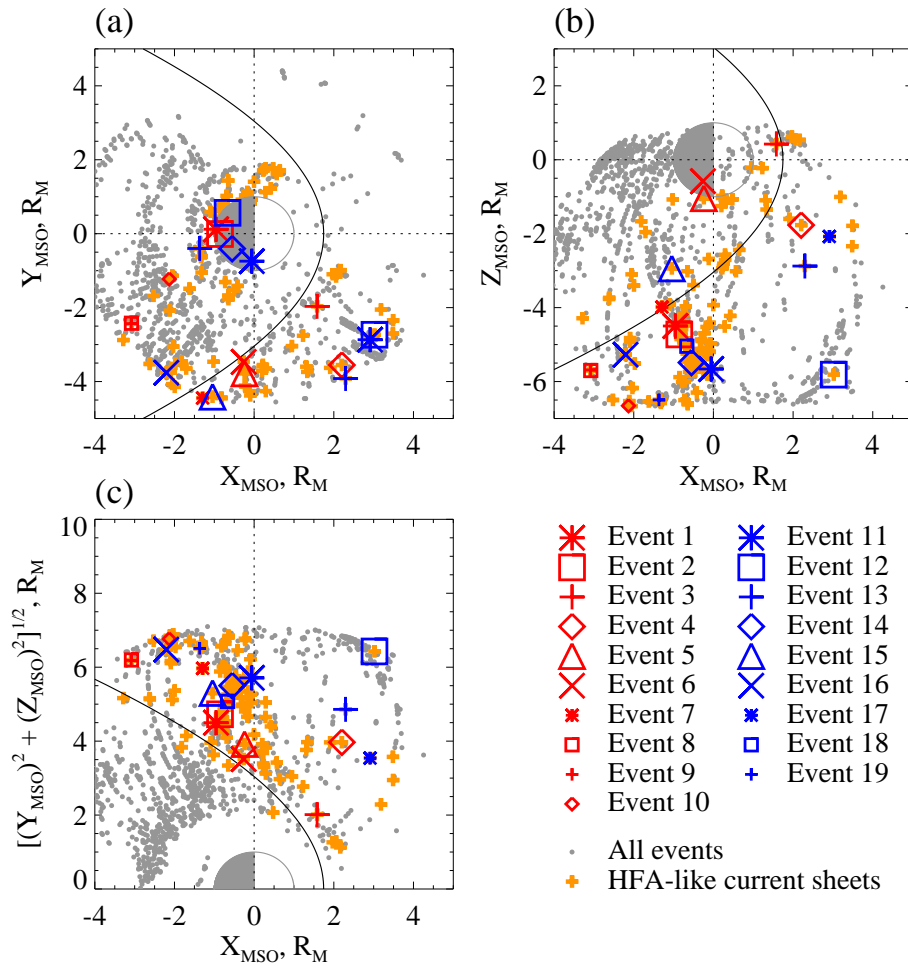
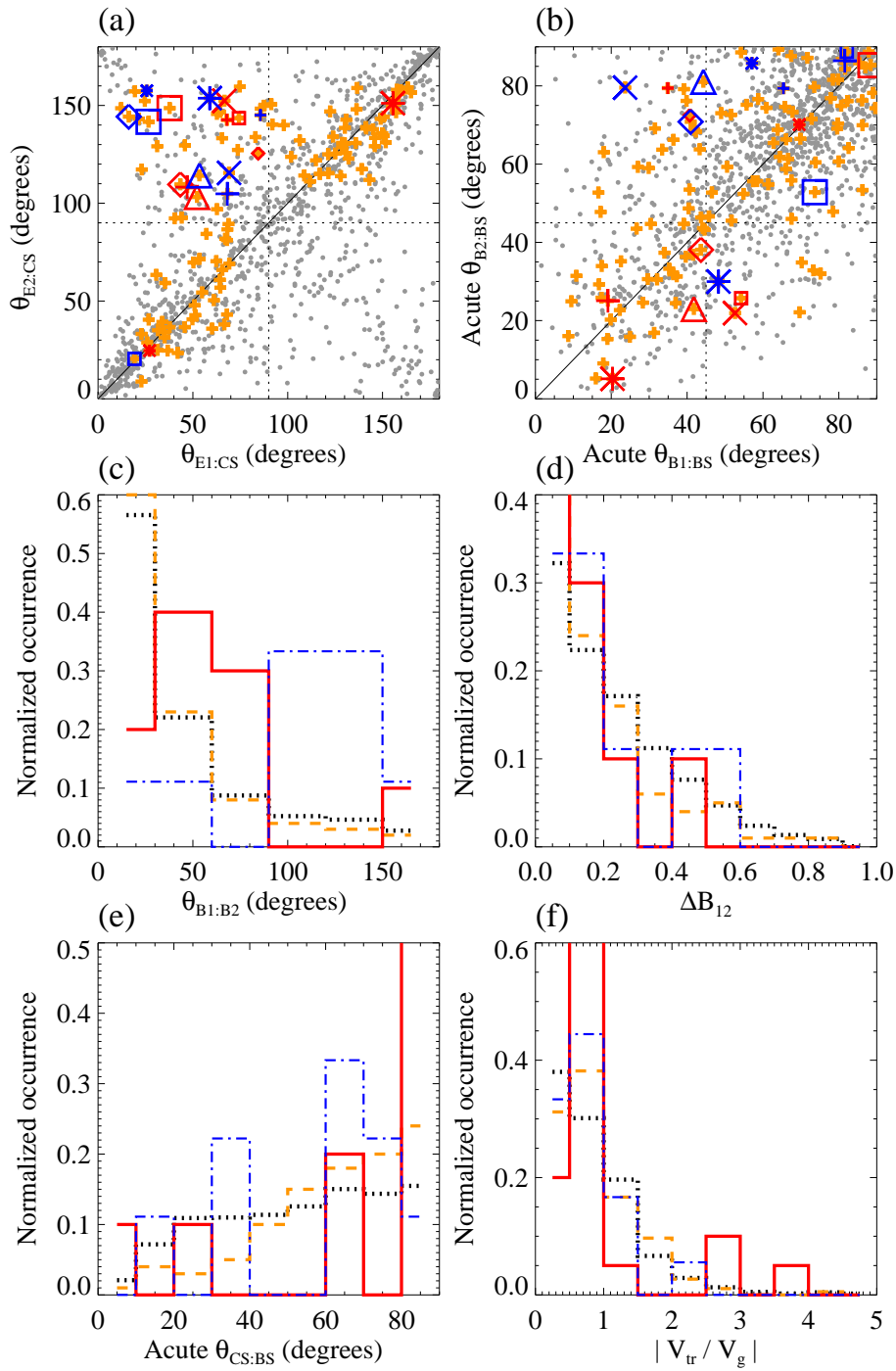


Figure 12. Examples of heliospheric current sheets in an upstream foreshock region.



**Figure 13.** Occurrence locations of the detected events. See text for details.



**Figure 14.** Statistical analysis of active current sheets in the Hermean foreshock; see Fig. 13 for symbol notations.

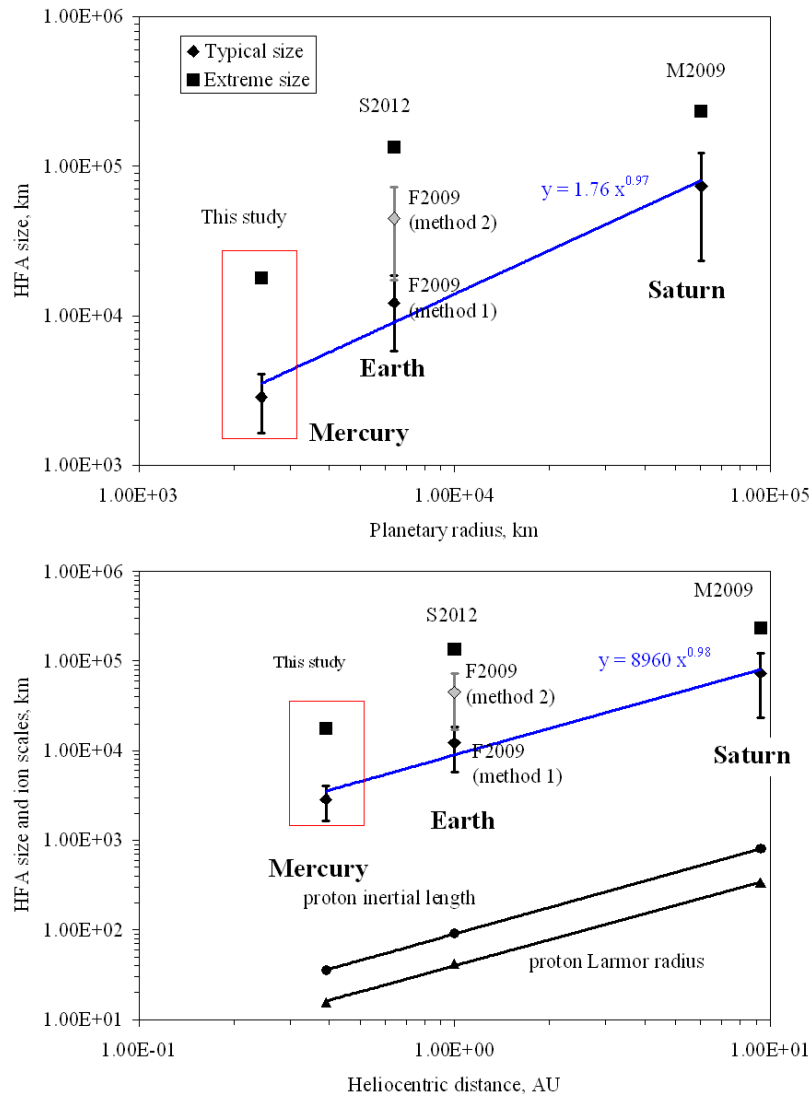


**Figure 15.** Estimated linear sizes of HFA events at Mercury as compared to the sizes of the HFA events at Earth and Saturn, as a function of planetary radius (top) and heliocentric distance (bottom). The typical sizes of terrestrial HFAs are adopted from *Facsco et al.* [2009] who used two complementary techniques (labeled as “method 1” and “method 2”) to get identify HFAs. The size of an extreme terrestrial event is taken from *Safrankova et al.* [2012]. The case studies published by *Masters et al.* [2009] were used to evaluate typical and extreme event sizes of HFA events at Saturn. The solid blue lines are the best power law fits to the data (excluding the method 2 - based estimate for terrestrial events). The ion scale plots are constructed using the statistical solar wind model by *Kohnlein* [1996]. The data suggest that the typical characteristic size of planetary HFAs is approximately 1.2 planetary radii which could be a combined effect of the bow shock geometry and the increase of the proton scales with the distance from the Sun.

